Characterization of the air flow in a scale model of a hydrogenerator by means of particle image velocimetry

Emmanuel BACH

Master of Science

Department of Mechanical Engineering

McGill University

Montreal,Quebec

May 2015

A Thesis submitted to McGill University in Partial Fulfillment of the Requirements of the Degree of Master of Engineering

ACKNOWLEDGEMENTS

I would like to thank my supervisors Professor Laurent Mydlarski, from McGill University, and Federico Torriano, from Hydro-Québec. Laurent Mydlarski offered me this opportunity and his support during two years. Federico Torriano gave me a passionate challenge and trusted me for the planning of the experiments. I am especially grateful for their careful reviews of the manuscript of this thesis and the article submitted during this project. I also want to thank Jean-Philippe Charest-Fournier who helped me in all my experiments, who prevented a lot of problems and resolved more. It would be impossible for me to reach these results without him. Numerous and various other people from the Institut de Recherche d'Hydro-Québec (IREQ) also contributed to my results. In particular, I would like to thank Hubert Sirois and Maxime-Olivier Jutras for the design and the construction of key mechanical components such as the laser support, essential to good quality measurements; Jean Picard, who conducted an important part of the measurements with me; Claude Hudon who lead this project; Jean-François Morissette who always provided me helpful advice; and all the people of the group who provided such a pleasant working environment. Moreover, I would like to thank the CRSNG (Conseil de Recherche en Sciences Naturelles et Génie), the FQRNT (Fonds Québécois de la Recherche sur la Nature et les Technologies) and Hydro-Québec for their financial support. Finally, I want to thank Camille Froger for her continuous support during these two years.

ABSTRACT

In hydroelectric power plants, generators are essential components and, like all machines, generate heat due to losses. The most common way to evacuate this heat is by circulating a cooling fluid (generally air) through the generator components. Due to their geometrical complexity, it is quite challenging to numerically simulate the flow to predict the cooling in a generator. Furthermore, *in situ* measurements are costly and difficult to perform due to the limited access. For this reason, a 1:4 scale model of a hydroelectric generator was built at the research institute of Hydro-Quebec (IREQ). In this thesis, particle image velocimetry (PIV) measurements of the flow in the opening of the generator pit, in the space between the enclosure wall and the cooler exit of the scale model, at the cooler exit, in the covers, and in the air gap and interpole region are presented. Experimental aspects pertaining to the seeding of the flow, calibration targets, experimental method and PIV theory are also discussed. Furthermore, a comparison of the experimental data with the results of CFD (Computational Fluid Dynamics) simulations using ANSYS-CFX is given. The results in the pit opening region have shown the sensibility of the simulation results to small modifications to the geometry. The measurements in the space between the cooler exit and the enclosure wall and those in the air gap and interpole region have qualitatively validated the CFD. Finally, computation of the mass flow rate through the cooler exit and in the cover has also quantitatively validated the simulation results.

ABRÉGÉ

Au sein des installations hydro-électriques, les alternateurs sont des composants essentiels et génèrent de la chaleur par pertes. Le moyen le plus courant d'évacuer cette chaleur est de faire circuler un fluide refroidissant (en règle générale de l'air) dans les différents composants de l'alternateur. En raison de sa complexité géometrique, il est très difficile de simuler cet écoulement afin de prédire l'efficacité du refroidissement. Par ailleurs, les mesures in-situ sont coûteuses et difficiles à réaliser en raison de l'accès limité. Pour ces raisons, un modèle à l'échelle 1:4 d'un alternateur hydro-électrique a été réalisé à l'institut de recherche d'Hydro-Québec (IREQ). Dans ce mémoire, nous allons présenter des mesures par Vélocimétrie par Image de Particules (PIV) dans les fosses alternateurs, dans l'espace entre les sorties radiateurs et la paroi de l'enceinte, à la sortie du radiateur, dans les capots ainsi que dans l'entrefer et l'interpôle. Les aspects experimentaux de l'ensemencement, de la calibration et de la méthode de mesure ainsi que les aspects théoriques de la PIV sont étudiés. Par ailleurs, une comparaison avec des résultats de simulation CFD ("*Computational Fluid Dynamics*") réalisée à l'aide d'ANSYS-CFX est également présentée. La sensibilité de la simulation aux modifications géométriques a été mise en avant grâce aux mesures réalisées dans la fosse alternateur. Les mesures conduites dans l'espace entre la sortie radiateur et la paroi de l'enceinte ainsi que dans l'entrefer et l'interpôle ont permis de valider qualitativement la CFD. Enfin, le calcul du débit d'air massique à travers la sortie radiateur et dans les capots ont permis de valider quantitativement les résultats de la simulation.

TABLE OF CONTENTS

LIST OF TABLES

LIST OF FIGURES

LIST OF SYMBOLS

- C = correlation function
- $C_{p,air}$ = Heat capacity of the air
- $C_{p,water}$ = Heat capacity of the water
- d = cylinder diameter
- d_e = diameter of PIV particles seen by the camera due to diffraction
- d_p = diameter of PIV particles
- D_0 = peak detectability
- e = air gap distance
- f = focal length of the laser sheet lens
- F = Fast Fourier Transform function
- F_0F_1 = mean fraction of particles that remains into the interrogation window between the two pulses
- f_s = shedding frequency
- $I(m,n)$ = light intensity received by pixel (m,n)
- L = characteristic length of the flow
- Ma = camera magnification
- $\dot{m}_{air}$ = air mass flow rate
- $\dot{m}_{water}$ = water mass flow rate
- N_1 = mean number of particles in an interrogation window
- N_L = mean number of particles in an interrogation window visible by the camera
- No = camera aperture
- p = dynamic pressure
- R = cross correlation function
- r, σ_s, r_c = residual, normalization vector and threshold in the universal outlier detection
- Ra_0 = Rayleigh length of the camera
- Re = Reynolds number
- r_m = radius of the model
- RPM = revolutions per minute
- r_r = radius of the real generator
- St = Strouhal number
- Sto = Stokes number
- TBP = time between laser pulses

- T_{in} = inlet temperature
- T_{out} = outlet temperature
- U_{∞} = freestream velocity
- u,v and w = air velocity along the x, y and z axis
- $\delta_{m,n}$ = Kronecker symbol
- Δt = time between laser pulses
- Δx = mean displacement of an interrogation window
- Δx_0, Δx_i = particular displacement
- Δx_m = median displacement
- Δz_0 = minimum thickness of the laser sheet
- η = average projection error of the calibration
- μ = dynamic viscosity
- μ_m, σ = mean value and standard deviation of a Gaussian probability distribution
- Φ = potential of the volumetric forces applied on the fluid
- ρ = density
- ρ_p = density of PIV particles
- ω_m = angular velocity of the scale model
- ω_r = angular velocity of a real generator

Chapter 1
Introduction

1.1 Hydroelectricity in Québec

The province of Québec owns important water resources. Indeed, one can count more than 4 500 rivers and 500 000 lakes on its territory. This motivated Hydro-Québec to build 60 power plants with a production capacity of 35337 MW (as of November 11, 2014), which represents 98% of the electricity production by Hydro-Québec.

One of the key components in a power plant is the turbine-generator group. The turbine extracts kinetic energy from the water fall and transmits it to the generator which transforms it into electric energy (see Fig. 1–1).

Although generators have efficiencies greater than 95%, a part of the energy to be transformed is invariably lost as heat. Thus, the machinery needs to be cooled to prevent the electrical components from overheating. Usually, the cooling is done by convecting air into the various components. By rotating, the generator acts like a fan, but a compromise has to be found between generating a powerful flow, supplying efficient cooling and the minimization of the energy lost by this cooling flow. Indeed, the latter represents between 20% and 30% of the total losses. Therefore, the efficiency of the cooling is a important factor to consider when aiming to improve the efficiency of a generator.

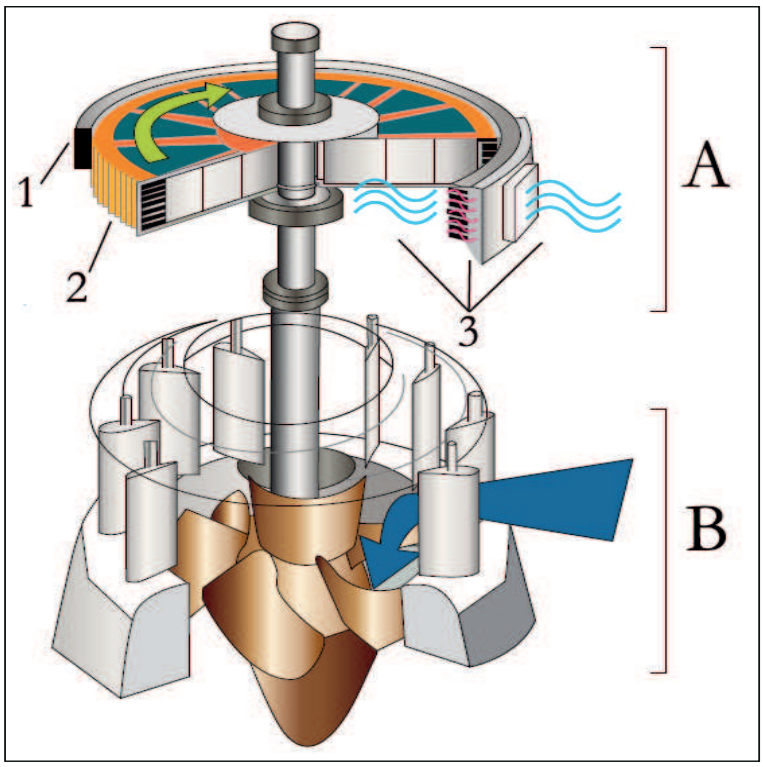

Figure 1–1: Turbine (B) generator (A) group where one can see the stator (1), the rotor (2) and the ventilation flow (3), from [42].

1.2 The AUPALE project

The majority of hydroelectric plants were built in the 1970s. At that time, the engineers were not able to predict precisely the behavior of the diverse components since they did not have access to the computational tools available nowadays. Consequently, generators were designed with large factors of safety. Using numerical simulation and new techniques, this margin can be reduced, which may allow an increase in production capacity without building new power plants. To reach this goal, Hydro-Québec launched the AUPALE project in 2002. This name is an acronym in French for increasing of the power of the existing generators (AUgmentation de

Puissance des ALternateurs Existants). A broader description of this project and related results was published by Hudon *et al.* [16]. An overview of the project is illustrated in Fig. 1–2.

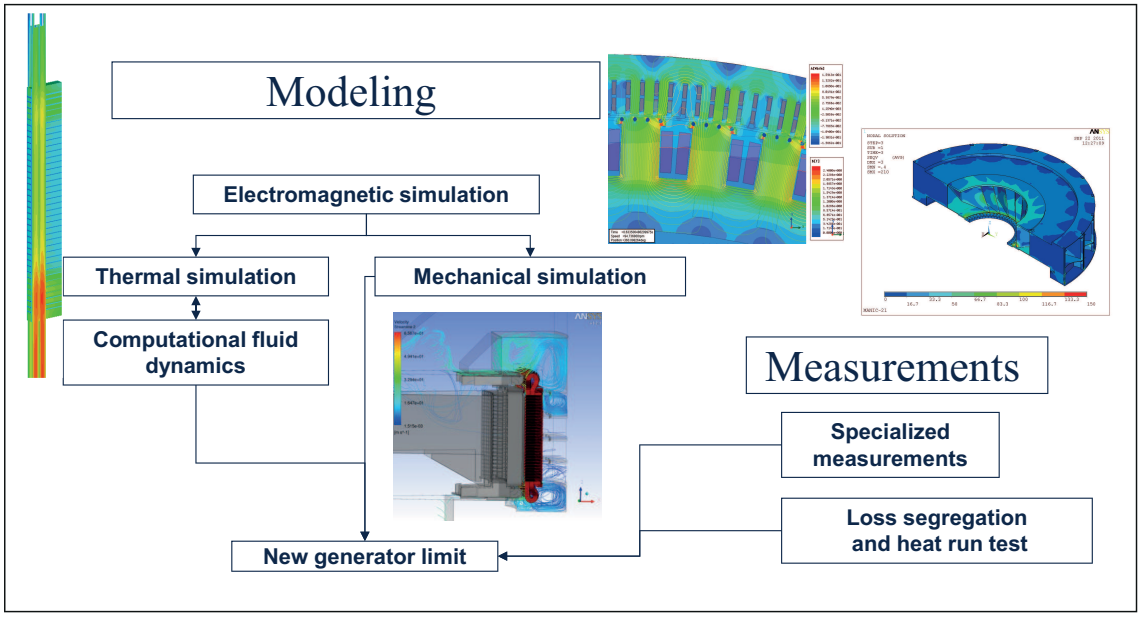

Figure 1–2: The AUPALE project.

Using a commercial code, the electromagnetic and mechanical loads have been computed. From the electromagnetic losses, the generated heating is determined and the final step is to determine the component temperatures to predict the new generator limit. The thermal analysis requires a thermal simulation, focusing on the temperature in the solid components, and a flow analysis, focusing on the air flow around and/or through each component. Such a simulation has been undertaken by Lancial *et al.* [23] and Torriano *et al.* [41], who validated their results with

measurements on a scale model built at the Institut de recherche d'Hydro-Québec (IREQ).

The related Computational Fluid Dynamics (CFD) analysis has already been undertaken by Toussaint as part of his master thesis [42]. His work, however, underwent no experimental validation. To rectify this, the IREQ built a simplified scale model of a generator. Already used for the thermal validation, this model was also partially built with transparent materials to allow optical access to permit optical flow measurements such as particle image velocimetry (PIV).

1.3 Objectives of the present research

In the context of the AUPALE project, experimental characterization of the air flow through a generator is needed to validate CFD simulations. The main aim of the present research is to measure the velocity fields to validate the CFD simulations in the complex flows that exist within a generator. The scale model, built with transparent materials to allow optical measurements, is used to this end. Particle Image Velocimetry (PIV) was mainly employed since this method has two advantages:

- It is a non-intrusive technique.
- The velocity field is obtained over a plane (as opposed to only at a single point), which allowed us to also compute mass flow rates.

However, as will be discussed in Chapter 3, PIV measurements are not without challenges, the main ones being the:

- seeding of the flow with the appropriate density of particles (oil droplets) in the measurement area without polluting the complete machine,

- existence of both rotating and fixed parts, and
- precision of the position of the camera and the laser in a scale model of a large size (3 m diameter, 2 m height).

Although the PIV system was already purchased, the present project was the first to use it at the IREQ. Thus, a significant amount of time was dedicated to developing and building a reliable experimental setup, and learning how to obtain high quality measurements with the help of Jean-Philippe Charest-Fournier, a technician at the IREQ.

Chapter 2
Airflow within generators

Due to its complex geometry, the details of the air flow within a hydrogenerator are relatively unknown. The main flow pattern is represented in Fig. 2–1. The rotor spider arm (1) acts like a pump that first drives the flow through the rotor rim and the fan blades (2), then through the air gap, the stator (3) and the covers (4). The flow is then convected through the stator frame (5) and the coolers (6). Finally, the air returns to the rotor through the top and pit openings (7).

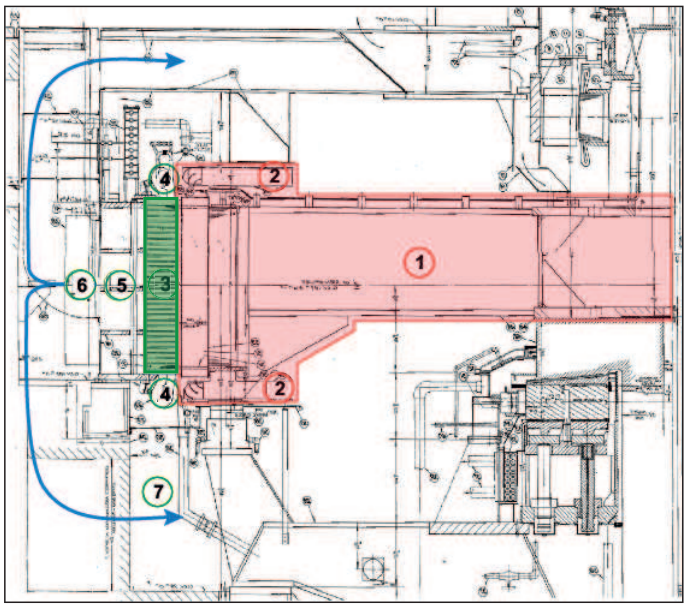

Figure 2–1: Schematic of the air flow through the rotating (red) and stationary (green) parts of a generator.

Given the complex geometry combined with the existence of both stationary and rotating parts, the flow in a generator is difficult to simulate. As it is also difficult to access to the generators during their operation, experimental measurements are very costly and difficult to perform. Since knowledge of the air flow in a generator is a key factor to improving the cooling in this machinery, notable efforts have been made in the last twenty years towards this end. A partial review is presented here, divided into experimental, network computation, and computational fluid dynamics works.

2.1 Experimental studies

Some experimental work has been undertaken in the past to obtain partial results, most notably the air flow through the cooler exits, as it usually is the most accessible part. This flow can be measured directly by integrating velocity profiles, or indirectly by thermal- or pressure-based approaches.

Integral approaches consist of scanning the flow area with an ANEMOMETER (hot-wire or Pitot tube) and integrating the result to obtain volume and mass flow rates. The weakness of this method is the fact that discrete single measurements are obtained to determine global mean quantities. Consequently, special attention must be given to the non-uniformity and non-stationarity of the flow. The most relevant references in the calculation of cooling air flows within generators using integral approaches are those of Filipan *et al.* [10] and Moradnia *et al.* [32].

Indirect methods are based on measurement of quantities other than the velocity to infer the flow rates. Knowing that the energy lost by the air is transferred to the

cooling water, the principle of conservation of energy can be applied to the radiator and results in:

$$\dot{m}_{air} C_{p,air} \left(T_{in,air} - T_{out,air} \right) = -\dot{m}_{water} C_{p,water} \left(T_{in,water} - T_{out,water} \right), \tag{2.1}$$

where $\dot{m}_{air}$ and $\dot{m}_{water}$ are the respective mass flow rates of air and water through the radiator, and T_{in} and T_{out} are the inlet and outlet temperatures of both fluids. Thus, knowing the mass flow rate of the water and the inlet and the outlet temperatures for the air and water, one can easily compute the mass flow rate of the air. However, as the specific heat capacity of water is larger than that of the air, the measurements of the water temperatures must be very precise to obtain accurate results. Note, however, that this method only gives a global mass flow rate, without knowledge of its values in the different parts of the radiator. For more details on this method, see, for example, the work of Chaaban *et al.* [7].

Lastly, characterization of the air flow using only pressure measurements has been performed. Such an approach was used Gunabushaman and Venkata Suresh [12]. Using Bernoulli's equation (2.2), one can compute the velocity with the pressure at a single point:

$$\frac{u^2}{2} + \frac{p}{\rho} + \Phi = \text{const.}, \tag{2.2}$$

where u is the velocity, p is the static pressure, ρ is the density, and Φ is the potential of the volumetric forces applied to the fluid. The constant can be computed at another point on the same streamline that is easier to measure, or determined

by a calibration. At the IREQ, a different pressure-based approach involving an integration duct has been employed. As shown in Fig. 2–2, an integration duct was connected to one channel of the stator by Hudon *et al.* [16]. The flow through the duct was determined by measuring the pressure differences between the two ports, and relating it to the flow rate by way of a calibration.

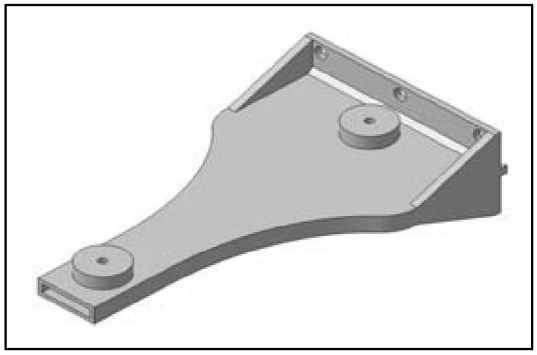

Figure 2–2: Flow measurements out of stator duct. (From [16]).

More recently, Hartono built a scale model of a generator as part of his masters studies [13]. He performed an experimental investigation using pressure measurements. Consequently, Hartono *et al.* [14] used this model to make PIV measurements to investigate the air flow outside the stator and inside the rotor channel.

2.2 Network computations

Flow network analysis can be considered a part of a thermal network analysis. As the main objective of these analyses is to compute the maximum temperatures, they have been employed to conduct thermal analyses of electric machines and a useful summary of such approaches can be found in the paper by Boglietti *et al.* [5].

The lumped-parameter thermal-network (LPNT) is a method that provides relatively good results using computationally short simulations. However, its main

weakness is its strong dependence on the choice of the different heat transfer coefficients employed. Given that forced convective heat transfer coefficients are a function of the local velocity, a flow-network analysis technique has been developed to also predict the fluid velocity. This method is fully explained in the paper by Staton and Cavagnino [39]. Based on an analogy with an electrical circuit, all components involved in the air flow are represented by equivalent electrical components. A flow resistance becomes an electrical resistance, a channel becomes an inductor, and the network represents the geometry. Knowing them, an electrical analysis gives the current (i.e. volume flow rate), and the voltage (i.e. pressure drop) in each part of the generator. A flow network, combined with a heat transfer network is called a thermal network and gives results within 10% of the measurements, given the proper modelling and the correct characteristics of each component. However, this approach still depends on the specification of the characteristics of each component, which are generally determined by computational fluid dynamics simulations.

2.3 Computational fluid dynamics simulations

Computational Fluid Dynamics (CFD) simulations solve the conservation equations after discretizing them in time and space. However, this technique is very expensive in term of numerical resources. Indeed, the size of the machinery is a factor, but there are also very small elements, requiring fine meshes. The required number of cells is thus enormous (typically more than 10^7) and simulations of the whole machine are very rare in the literature. Consequently, CFD is used only on certain components to determine the heat transfer coefficients and fluid resistances used into the network techniques (see, for example, Hemery and Kunz [15]). This

being said, local studies have also led to the improvement of particular aspects of the cooling airflow (see, for example, Depraz *et al.* [8]). Finally, it should be noted that a complete simulation of an entire hydroelectric machine was undertaken by the IREQ [42]. However, a detailed experimental data set does not exist, so these simulations have not been validated. This fact serves as the principal motivation for this research.

Chapter 3
Particle Image Velocimetry

3.1 General principle

PIV refers to a class of methods used in experimental fluid mechanics to determine instantaneous velocity fields by measuring the displacement of numerous fine particles that closely follow the motion of the fluid. With 2D PIV, it is possible to measure two components of the instantaneous velocity in a plane. Thus, one can obtain mass flow rates by integrating velocities over several planes.

Like a child who throws a piece of wood in a river to follow it in the stream, PIV is based on the seeding of visible tracers (seeding particles) in a flow. Illuminating them with a pulsed laser, and recording two images of the particles at each of the two pulses that are separated by a known time interval, one can infer the fluid velocity. A representation of the PIV approach to acquiring images is shown in Fig. 3–1.

Once the images are acquired, they are subdivided into small interrogation windows. These areas are enough small to assume that all the particles inside them have the same velocity. The particles are chosen to scatter the light, thus they are identified by bright spots in the images. By correlation of the light intensity between the two images, the mean displacement of the interrogation window is computed. With the displacement and the time interval, one obtains the velocity in the window. As the time between pulses is short, we can assume that this velocity is the instantaneous velocity at the time of the first pulse.

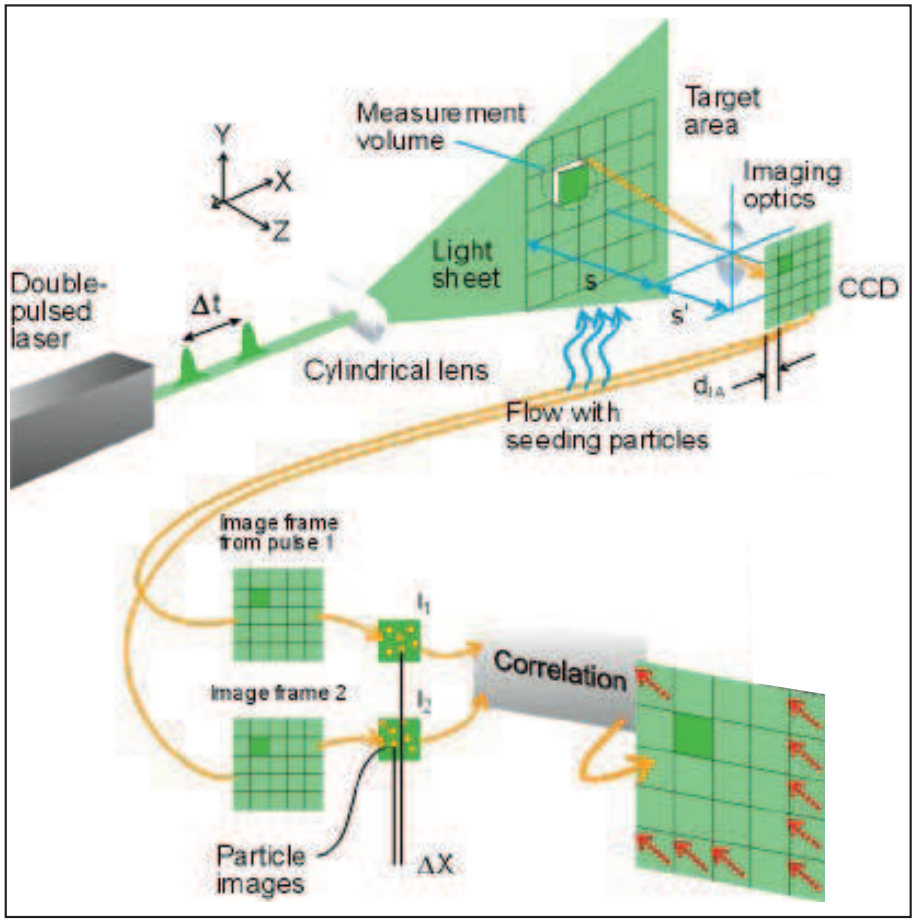

Figure 3–1: Elements in a planar two-dimensional particle image velocimetery system, from Dantec Dynamics website.

3.2 Main Components

3.2.1 Seeding of the flow

The seeding of the flow is a key aspect in a PIV measurement. A particle needs to be big enough to scatter a sufficient quantity of light toward the camera, yet small enough to closely follow the motion of the fluid without perturbing it. In water, appropriate particle selection is relatively easy due to the high density of the

liquid. This allows particle sizes as large as 30 μm. Larger sizes would result in image superposition between two neighboring pixels on the CCD sensor. Indeed, as the laser sheet has a non-zero thickness, two particles at different distance from the sensor can have their image superimposed. Conversely, in air, it is impossible to find particles with the same density as the fluid. So, the particles need to be very small, between 1 and 10 μm, such that $Sto << 1$, to follow the fluid.

To allow a precise determination of the velocity when using cross-correlation analysis, the number of particles needs to be sufficiently large. Keane and Adrian [19] explored the influence of this parameter in the graph presented in Fig. 3–2.

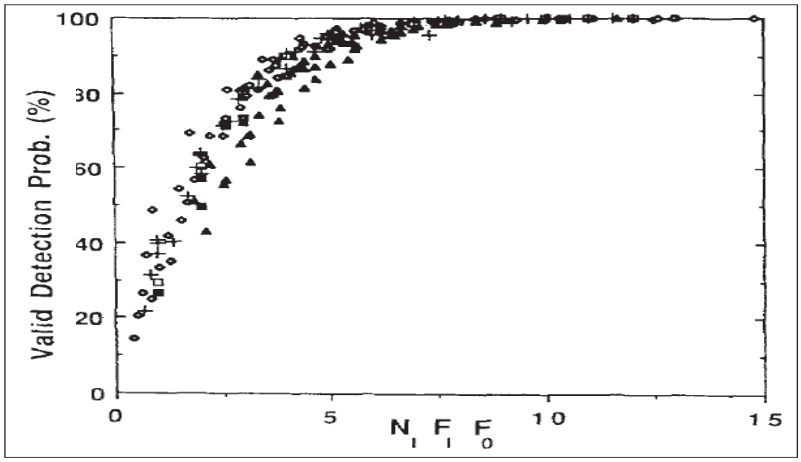

Figure 3–2: Evolution of the accuracy of the cross-correlation as function of the number of particles in one interrogation window, from [19].

In Fig. 3–2, F_0 is the mean fraction of particles in an interrogation cell that remain within the light sheet after moving perpendicularly to the light sheet, F_1 is the mean fraction of particles in an interrogation cell that remain within the interrogation window after moving in the plane parallel to the laser sheet, and N_1 is the mean number of particles in an interrogation window in the first image. Thus,

$N_1 F_0 F_1$ is the mean number of particles remaining in the interrogation window after the particles' displacements. One can see in Fig. 3–2 that 10 or more particles remaining in the interrogation window are needed:

$$N_1 F_0 F_1 \leq 10. \tag{3.1}$$

On the other hand, the density of particles has to be low enough to avoid overlap. Adrian [1] quantified the mean number of particle images that overlap by:

$$\text{SD} = N_L \Delta z \left(\frac{d_e}{Ma} \right)^2, \tag{3.2}$$

where N_L is the mean number of particles per unit volume that are large enough to be visible by the camera, Δz is the laser sheet thickness, d_e is the particle diameter (including diffraction) and Ma is the camera magnification. d_e can be estimated from the particle diameter and the camera geometry by:

$$d_e = \sqrt{Ma^2 d_p^2 + \left(2.44(1+M)\frac{f}{\text{No}}\lambda \right)^2}, \tag{3.3}$$

where f and No are the focal length and the aperture of the camera, respectively, and λ is the wavelength of the illumination. To obtain a high quality image for PIV, SD must be much smaller than one. Given the size of the scale model in the present work, the main difficulty was to obtain a sufficient particle density, not avoiding superposition. Thus, the previous criteria, $SD << 1$, was always satisfied.

The challenge thus became the generation of the right density of particles of the right size. Moreover, the particles need to be non-toxic, non-corrosive, non-abrasive,

non-volatile and chemically inert. Knowing that, the most commonly used particles in PIV measurements in air are summarized in Table 3–1.

Table 3–1: Seeding materials for gas flows, from [34].

Type	Material	Mean diameter (μm)
Solid	Polystyrene	$0.5 - 10$
	Alumina Al_2O_3	$0.2 - 5$
	Titania TiO_2	$0.1 - 5$
	Glass micro-spheres	$0.2 - 3$
	Glass micro-balloons	$30 - 100$
	Granule for synthetic coatings	$10 - 50$
	Dioctylphathalate	$1 - 10$
	Smoke	< 1
Liquid	Different oils	$0.5 - 10$
	Di-ethyl-hexyl-sebacate (DEHS)	$0.5 - 1.5$
	Helium-filled soap bubbles	$1000 - 3000$

Because of their low price and their ease of use, oil droplets were selected. They can be generated by way of a seeding generator (Laskin [24]), described in Fig. 3–3. Such an atomizer produced oil droplets between 1 and 10 μm, with an impactor plate to remove overly large particles. From the results of Kähler *et al.* [18], one can see that the size distribution of the droplets is a good comprise between scattering and non-disturbance of the flow. Their main drawback, however, is the resulting oil deposit on every surface, requiring regular cleaning of the scale model.

3.2.2 Lighting system

The use of small tracer particles in PIV measurements requires the use of an intense light source. The most common choice, and also our choice, is a double-pulsed

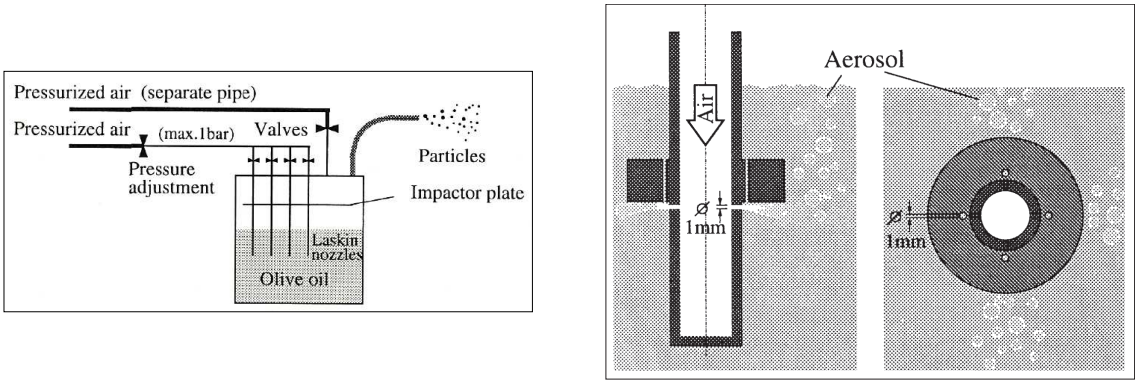

Figure 3–3: Laskin oil generator, from [34].

Nd:YAG laser. Described in detail by Adrian and Westerweel [3], the double-pulsed Nd:YAG laser can generate a pair of pulses at a maximum frequency of 7.4 Hz with a wavelength of 532 nm.

To transform the laser beam into a light sheet, it is necessary to use a cylindrical lens to spread the beam with a chosen angle and a spherical one to adjust its thickness. Their arrangement is depicted in Fig. 3–4.

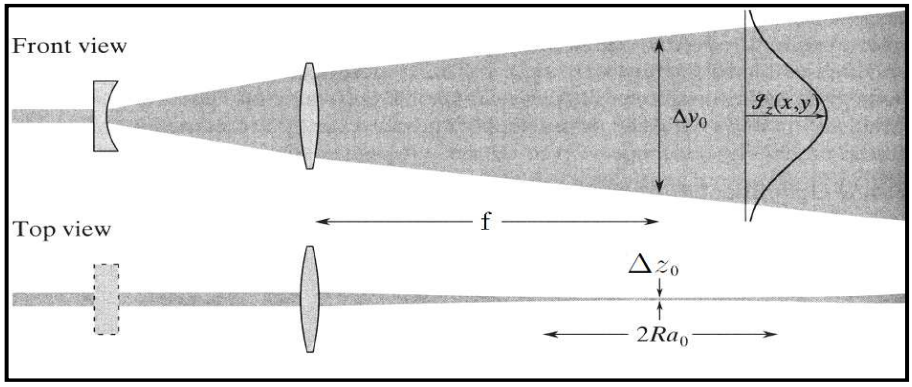

Figure 3–4: Light sheet formation using a cylindrical and a spherical lens, from Adrian and Westerweel [3].

This system allows the specification of the sheet thickness to ensure that more than 75% of the particles remain in the light sheet between the two laser pulses. However, from Fig. 3–4, one can observe that the measurement area must be limited to a region around the focal length f of the lens, to ensure minimal variations in thickness of the sheet over the measurement area. Historically, this thickness is considered to be effectively constant in the range $[f - Ra_0, f + Ra_0]$, where Ra_0 is the Rayleigh length, defined by $\Delta z \leq \sqrt{2}\Delta z_0$ with Δz_0 being the minimum sheet thickness (from Adrian and Westerweel, [3]).

Finally, the contrast between particles and the background must be as large as possible. To this end, the double-pulsed laser must be powerful, and the noise level must be low. Moreover, all reflections and external sources of light must be removed.

3.2.3 Camera

Recording the images used in PIV poses a number of challenges, that are defined by the requirements that the camera and recording system meet the following characteristics :

- The buffer disk must record two images separated in time by few microseconds. Thus, a temporal buffer system, which can save the first image for a short time, is required. The solution is the progressive scan interline transfer CCD (Charged Coupled Device), described by Lai *et al.* [21]. Such a CCD sensor has one buffer layer for each pixel, as shown in Fig. 3–5. This CCD sensor permits time intervals between pulses as small as 0.38 µs.
- The number of pixels on the CCD sensor must be large enough so that the particle size is between 2 and 3 pixels. This bound is required to both precisely

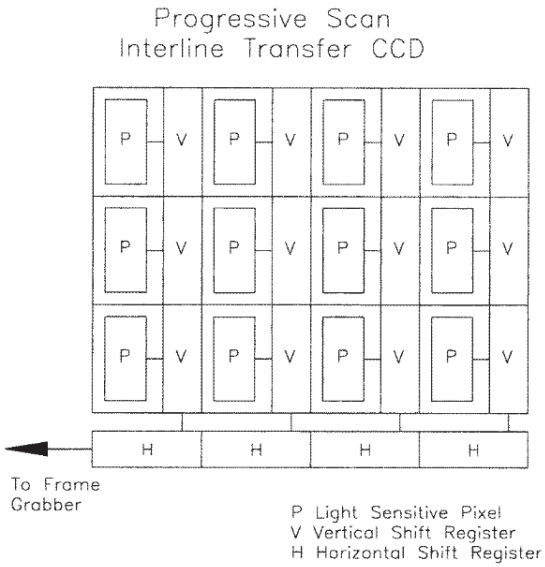

Figure 3–5: Progressive scan interline transfer CCD architecture, from Lai *et al.* , [21].

determine the particles' positions and to avoid their superposition. When determining the size of a particle on the CCD sensor, diffraction must also be taken into account.

- The depth of field of the camera must be large enough for all particles in the laser sheet to be in focus.

3.2.4 Synchronization

The synchronization between the laser, the camera and the buffer is performed by a timing box. The timing diagram, which accounts for the delays for transmitting an electrical signal through the different connections, is depicted in Fig. 3–6. In this figure, an active component is represented with a high value. The time delays depicted are the minimum possible ones by our Dantec system. The external signal is sent by the timer box and launches the image capture. As there is a minimum

opening delay, the camera diaphragm opens itself for image A and the laser flashes at the end of the exposure. The camera diaphragm closes, the image is immediately transferred to interline register (cf Fig. 3–5), and the diaphragm opens again for the second image. The laser flashes at the beginning of the exposure to reduce the time interval between images. At this time, the camera needs to wait for the transfer of image A from the interline register to the computer before transferring image B.

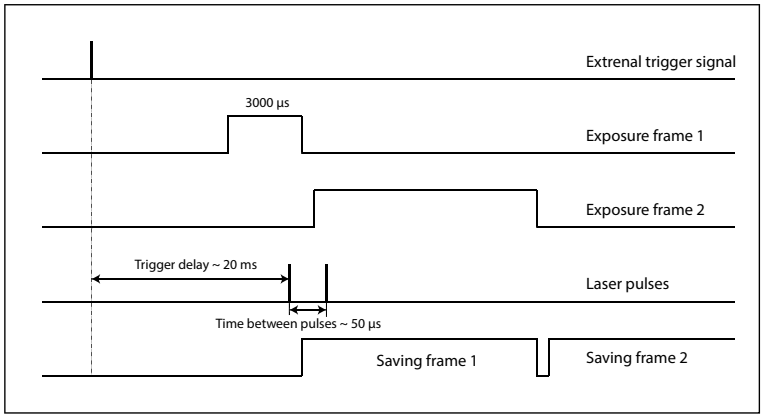

Figure 3–6: Typical timing diagram for a PIV system using dual-frame digital camera, from Lemay [25].

3.3 Calibration

Calibration of the entire system is required to convert the image on the CCD sensor into an image that represents the true location of the particles. As the optical path can be very complicated, a calibration procedure is used to determine the mathematical relationship between the image of the object on the CCD sensor and the real object. To this end, a calibration target is put at the measurement area and an image is recorded. As the exact dimensions of the target are known, the PIV software determines the mathematical operation to convert the image on the CCD

sensor to the real calibration target. This equation will then be applied to each image in the post-processing procedure. The function that relates the real coordinates into the image coordinates is a third-order quadratic polynomial (Soloff *et al.* , [36]):

$$\begin{aligned} \vec{x}_{CCD} &= \vec{a}_0 + \vec{a}_1 x + \vec{a}_2 y + \vec{a}_3 z + \vec{a}_4 x^2 + \vec{a}_5 xy + \vec{a}_6 y^2 + \vec{a}_7 yz \\ &\quad + \vec{a}_8 z^2 + \vec{a}_9 xz + \vec{a}_{10} x^3 + \vec{a}_{11} x^2 y + \vec{a}_{12} xy^2 + \vec{a}_{13} y^3 \\ &\quad + \vec{a}_{14} x^2 z + \vec{a}_{15} xyz + \vec{a}_{16} y^2 z + \vec{a}_{17} xz^2 + \vec{a}_{18} yz^2. \end{aligned} \tag{3.4}$$

To evaluate the 19 vector coefficients (38 scalars), the software needs a predefined grid. Usually, the calibration target consists of a regular grid of markers with a precisely known spacing, such as a grid of dots with a larger dot at the origin and smaller dots for the axes. Fig. 3–7 shows the calibration target with the grid computed by the DynamicStudio software after determination of the coefficients. The yellow dots represent the dots detected by the software and the grid is determined from the computed coefficients. If the computation is perfect, the grid will overlap with the dots. In figure 3–7, the correspondence is very good, indicative of a good-quality calibration. Moreover, the location of the origin and the determination of the axis, marked in red can also be checked. If it is needed, several image processes (such as improvement of the contrast or removal of the background noise) can be applied to improve the detection, thus improving the quality of the calibration.

In addition to the visual check of the calibration, there is a quantitative parameter: the average projection error η, quantified in pixels. This parameter is the standard deviation between the points and the grid nodes. It is commonly assumed

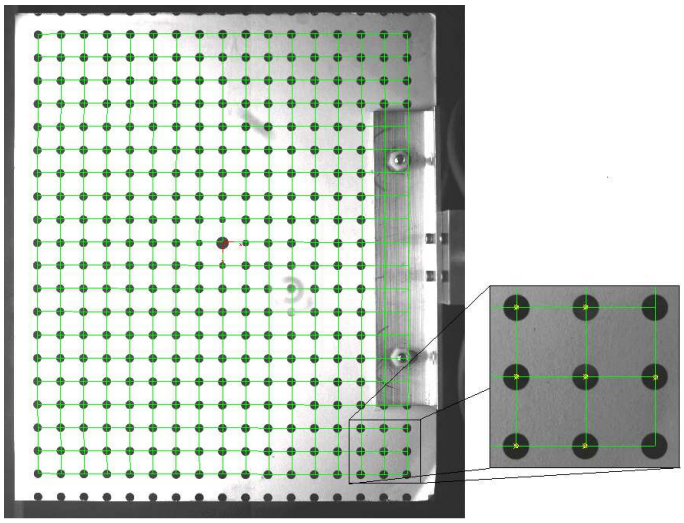

Figure 3–7: Calibration target (dots) and imaging model fit (grid).

that the calibration is accurate if $\eta \leq 0.5$ pixels. For the measurements presented herein, $\eta \leq 0.25$ pixels.

Finally, because of the size of the scale model and the restrictions to insert the calibration target in it, it was impossible to design a target that covers the most part of the image for the measurement in the space between the cooler exit and the enclosure wall. As it is risky to extrapolate the calibration outside the region covered by the target, the validity of the dewarping outside the target must also be checked. In this situation, two different calibration images are recorded with the target covering two different parts of the measured area. The results obtained from the two calibrations are shown in Fig. 3–8. A quantitative comparison gives a mean absolute error between the two results of 0.0437 m/s. This error is of the order of 0.02 m/s, the mean absolute error when all the components are perfectly positioned.

Consequently, this comparison allowed us to extrapolate our calibration outside the region covered by the target.

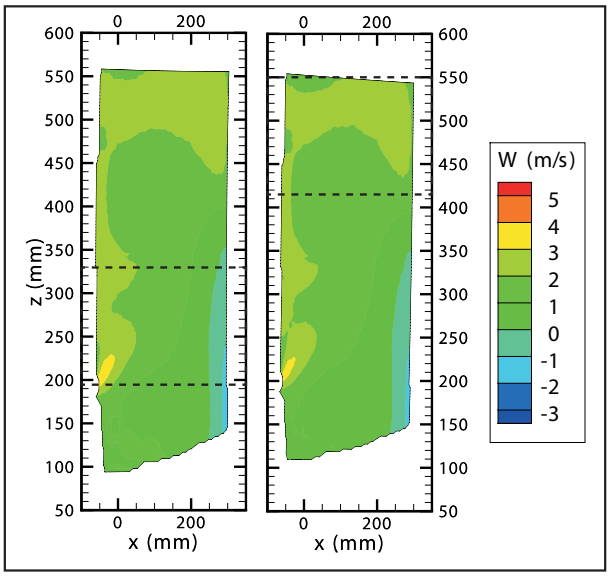

Figure 3–8: Velocity vector maps in the space between the cooler exit and the enclosure wall with two different calibration target positions indicated in dashed lines.

3.4 Post-processing

The interrogation process in high-density PIV is well described by Adrian and Westerweel [3]. Hence one can refer to their explanation as a basis for the description of the post-processing methods integrated in the DynamicStudio software.

3.4.1 Adaptive correlation

Cross-correlation

In high density PIV, it is no longer possible to identify each particle in a pair of images (as opposed to low density PIV). Therefore, it is necessary to adopt a statistical approach. This approach was first proposed by Soo *et al.* [38].

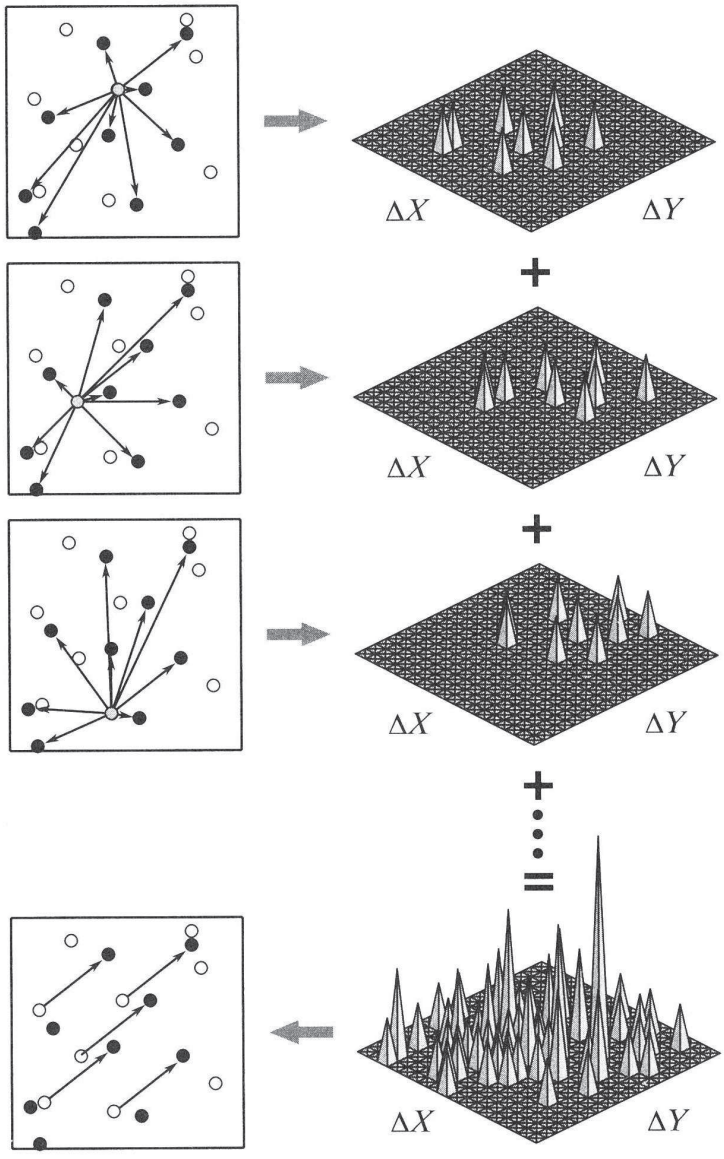

Figure 3–9: Principle of statistical analysis for PIV interrogation, from [3].

The principle of the statistical analysis is based on cross-correlation and is illustrated in Fig. 3–9. In this schematic, the particles seen in the first image are drawn in white and those in the second one are in black. In the image, every possible displacement is computed by making a correspondence for each particle between the first and the second time-frame. Each possible displacement is represented by a peak. Repeating this operation for all particles and summing the results, a cross-correlation histogram is obtained in which the real displacement is defined as the location of the tallest correlation peak. Mathematically, the cross-correlation is defined by the equation:

$$R(\Delta x) = \int I_1(x) I_2(x + \Delta x) dx. \tag{3.5}$$

However, this technique only works if all the particles have the same displacement in the image. Consequently, this computation must be applied to windows small enough to assume that the displacement is uniform in each one of them, but big enough to contain a sufficient number of particles.

Moreover, the correlation is never perfect because some particles exit from the interrogation window between the two pulses or because of background noise. As a result, the detection of the tallest peak can be difficult or, worse, the tallest peak may not represent the real displacement. Thus, the "peak detectability" D_0 is defined by the ratio of the amplitude of the tallest correlation peak to the amplitude of the second tallest peak.

$$D_0 = \frac{\text{amplitude of the tallest correlation peak}}{\text{amplitude of the second tallest peak}}. \tag{3.6}$$

In the present work, the displacement is rejected when $D_0 \leq 1.2$, as advised by Keane and Adrian [19].

Finally, given the displacement in each interrogation window, the instantaneous velocity field is easily obtained knowing the time interval between the two images.

Discrete correlation

In reality, the CCD sensor is not continuous, so that the data is in fact discrete. A computation made by Westerweel [45] gives a minimal resolution of 256×256 pixels for 1 mm^2 to obtain good-quality images of each particle. This resolution is very high and requires a very fine CCD sensor. However, the high wavenumber region only contains the detailed shape of the particles, and this information is not needed. Thus, the resolution can be limited to a smaller value and Westerweel proposed the value of 64×64 pixels for 1 mm^2. Our camera has a 2048×2048 pixels sensor and the CCD sensor is about 3×3 cm^2, thus Westerweel's recommendation is respected.

Even if the digitization is performed in a manner such that useful data is obtained, formulas must be defined for the analysis of the discretized data. The discrete-domain equivalent of equation 3.5 is:

$$R(p,q) = \frac{1}{M \times N} \sum_{m=1}^{M} \sum_{n=1}^{N} I_1(m,n) I_2(m+p, n+q), \tag{3.7}$$

where $I(m,n)$ is the energy received by one pixel and equal to:

$$I(m,n) = \int \int \delta_{m,n} I(x,y) dx dy, \tag{3.8}$$

where $\delta_{m,n}$ is equal to 1 on the pixel m,n and 0 elsewhere. Even though equation 3.7 can be computed directly, there is a faster approach using Fast Fourier Transforms:

$$R(\xi, \Psi) = F_1^*(\xi, \Psi) F_2(\xi, \Psi), \tag{3.9}$$

where the symbol $*$ denotes the complex conjugate, and $F_1(\xi, \Psi)$ and $F_2(\xi, \Psi)$ are the Discrete Fourier Transforms of each signal, defined by [3]:

$$F(\xi, \Psi) = \frac{1}{NM} \sum_{m \in M} \sum_{n \in N} I(m, n) exp \left[-2\pi i \left(\frac{m\xi}{M} + \frac{n\Psi}{N} \right) \right]. \tag{3.10}$$

The derivation of this equation and more details can be found in Adrian and Westerweel [3].

It must also be noted that the precision and the accuracy in the estimation of the particle image displacement are affected by the pixel resolution. To minimize this error, a subpixel refinement technique is employed (Westerweel, [45]). With this approach, a Gaussian curve is generated in the two directions by using the tallest peak and its neighbours, instead of simply detecting the tallest peak. The displacement is thus determined from the maximum of the Gaussian curve. The precision thus increases from 0.5 pixels to 0.05 pixels. The principle of subpixel refinement is illustrated in Fig. 3–10. The various methods to detect the peak are furthemore detailed by Adrian and Westerweel [3].

Adaptation of the interrogation window

As mentioned in section 3.2.1, an essential condition for accurate PIV measurements is to have more than 10 particles remaining in the interrogation window between the two laser pulses. This increases the window size and thus reduces the spatial resolution. One way around this is to move the interrogation window between the two images, for example with a simple offset. A rough displacement is determined

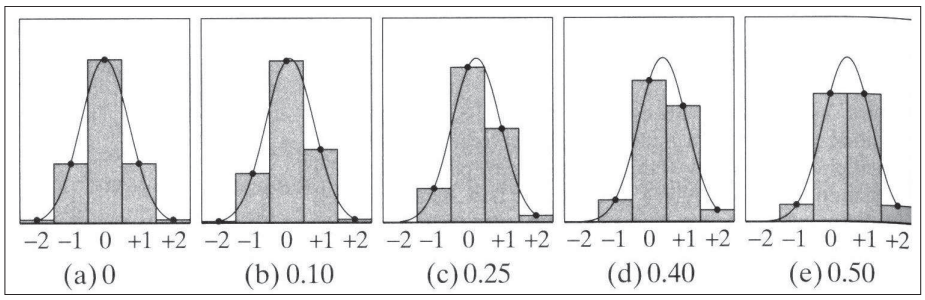

Figure 3–10: Detailed structure of discrete displacement-correlation peak for different values of fractional displacement (from [3], adapted from [45]).

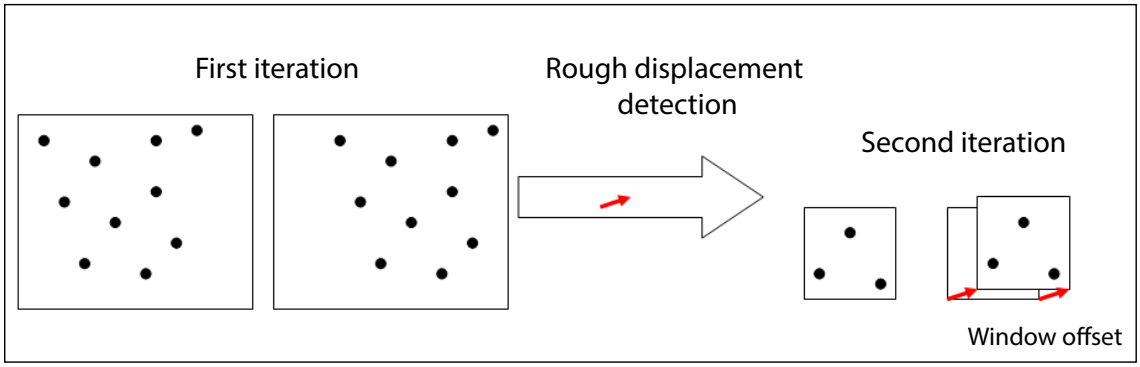

Figure 3–11: Iterative method to adapt the interrogation window to the flow field.

by a first cross correlation with larger windows. Then the window size is reduced and each window is translated by this displacement in the second image. A more precise velocity can then be computed. The principle of this method is illustrated in Fig. 3–11.

With the window offset, more particles can be captured, as seen in Fig. 3–11, while reducing the size of the interrogation area, thus increasing the spatial resolution of the measurement. This method has been used for each measurement in the present work with two successive window size reductions and two iterations for each size.

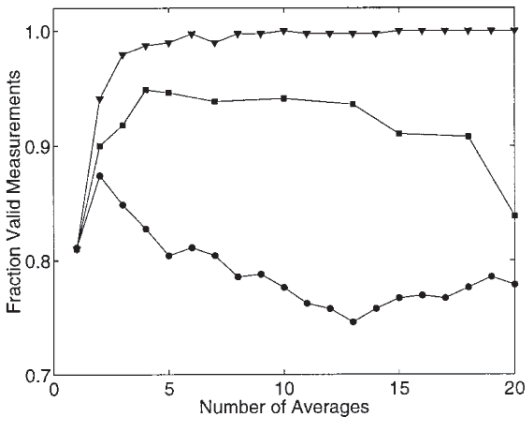

Figure 3–12: Percentage of valid measurements for the correlation averaging (triangles), the displacement averaging (circles) and the image averaging (squares), from [26].

Correlation averaging

As the main interest in the current study is the distribution of the mass flow rate of air in the scale model, the average velocity at each point has to be computed. To do so, one can average the images, the correlations or the velocity fields. The three different methods were compared by Meinhart *et al.* [26]. In the case of a good quality image with a sufficient number of particles, it was found that the three methods are equivalent. Moreover, as the averaging of the velocity fields allows several improvements in the analysis, such as adaptive correlation, it is the most frequently used method and was also chosen in the present work. However, for poor quality measurements, when the condition 3.1 is not satisfied, averaging the correlation is much more precise, as illustrated in Fig. 3–12.

3.4.2 Validation

Once the velocity field is obtained, one must validate each vector. Indeed, even if several techniques, described in section 3.4.1, increase the reliability of the velocity determination, there is a finite, non-zero probability of incorrectly determining the correlation peak. As the measured velocity field is supposed to have a certain "coherence," one can observe that a certain number of vectors are erroneous. To exclude such false data from the computation of the statistical quantities, they need to be identified through an automatic procedure.

Peak detection

The first validation step is performed during the peak detection process by way of the peak detectability defined in equation 3.6. This operation rejects all the vectors for which the tallest correlation peak is not sufficiently different from the second highest one.

Vector masking and masked correlation

Sometimes, there are unwanted objects in the image such as reflections, bounding walls or solid obstacles. Thus, the areas where it is impossible to detect a strong correlation peak must be masked. As the identification of the spurious vectors is based on their location, a mask is done on one image and applied to the entire vector field. There is no mathematical operation behind this validation. However, when the key vectors are near a masked area, this simple method can generate some errors. Indeed, with adaptive correlation, the first iteration was performed with relatively large interrogation windows that may contain unwanted objects. Consequently, the

light can reflected by these objects is included in the computation like particles and can generate a large error.

To solve this problem, Gui *et al.* [11] proposed a masked correlation. Applying the mask before the correlation and substituting masked areas with black ones reduces the effect of light from unwanted objects in the computation of the correlation. However, for interrogation windows that only cover unwanted objects, the computed displacement remains false. Therefore, a vector masking step is always needed. To save computational time, this step is not applied in the present work.

Universal Outlier Detection

Because of the "smoothness" of the flow that occurs in nature, a validation method based on the displacement of neighbouring points at a given time is reasonable. One of the first to propose such an approach was Westerweel [44]. Comparing three different methods based on the validation by a global mean, a local mean or a local median, the author concluded that the key quantity is the residual with respect to the local median:

$$r = \frac{|\Delta x_0 - \Delta x_m|}{\sigma_s}, \tag{3.11}$$

where Δx_m is the median displacement of the data in the neighbor of Δx_0, and σ_s is a normalization factor. When r is larger than a given threshold value r_c, the displacement Δx_0 is considered as a spurious vector.

The drawback of this technique lies in the choice of the normalization factor σ_s and the threshold value r_c. In the original paper, Westerweel [44] proposed the

simplest value $\sigma_s = 1$ with an adaption of r_c to the local properties of the flow. However, eleven years later, Westerweel and Scarano [46] proposed a universal method in which the value of σ_s is no longer taken equal to 1, but equal to the median of the neighbors' residuals: $\sigma_s = r_m$, the median of $r_i = |\Delta x_i - \Delta x_m|$ for $i \in \Omega$, where Ω is the set of neighbours. A small offset σ_ϵ is added to r_m to improve the performance, avoiding a divergence of r in case of very low fluctuation levels. Usually, as the precision of a PIV displacement measurement is of the order of 0.1 pixels, $\sigma_\epsilon = 0.1$ pixels is chosen. Consequently, the validation quantity becomes:

$$r = \frac{|\Delta x_0 - \Delta x_m|}{r_m + \sigma_\epsilon}. \tag{3.12}$$

The remaining difficulty is the proper choice of the threshold value r_c. Westerweel and Scarano [46] applied their method to a wide range of PIV data and concluded that the optimal value is universal. Westerweel and Scarano determined a common value for typical flows: $r_c = 2$. This value can be adjusted depending on the flow but it also appears to be the appropriate value in the present study and was therefore used during the validation procedure.

Although this method shows a good universality, one must keep in mind that this validation procedure is based on the data at neighbouring points. Thus, it is implicitly assumed that the spurious vectors are isolated. It therefore appears that the condition for an efficient and robust detection occurs when the fraction of spurious displacements in a PIV measurement is no more than about 5% of the total displacements.

N-Sigma validation

Different measurements at one point and at different times are repetitions of the same measurement. As only non transient flows were studied in the present work, these data should follow a probability distribution. Assuming that the data is normally distributed, the probability density function is given by:

$$f_n(v) = \frac{1}{\sigma\sqrt{2\pi}} \exp\left[-\frac{1}{2}\left(\frac{v-\mu_m}{\sigma}\right)^2\right], \tag{3.13}$$

where μ_m is the mean and σ the standard deviation of a series of M samples.

Even if the data are not normally distributed, all valid data should be in a range such that:

$$\left(\frac{v-\mu_m}{\sigma}\right)^2 = r^2 \leq N^2, \tag{3.14}$$

with $4 \leq N \leq 6$. Consequently, the vectors can be considered as spurious if they are out of this range. The value of N must be adjusted depending on the unsteadiness of the flow.

Fig. 3–13 depicts an example of applying the different validation procedures: 3–13a, the vector masking, 3–13b, the peak validation, 3–13c, the universal outlier detection and 3–13d, the N-sigma validation. The rejected vectors are shown in red.

3.4.3 Data replacement

After the identification of the spurious vectors, they are removed from the data set. As a result, the data set contains holes at the locations at which spurious data were removed. Consequently, they need to be replaced, to minimize the error on the vector statistics. The simplest method is linear interpolation. As spurious data are

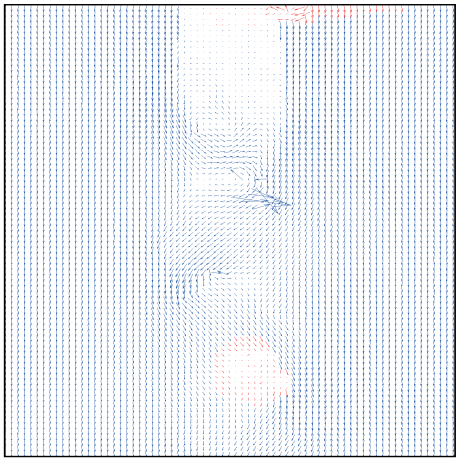

(a) Vector fields after applying the vector masking (341 rejected vectors).

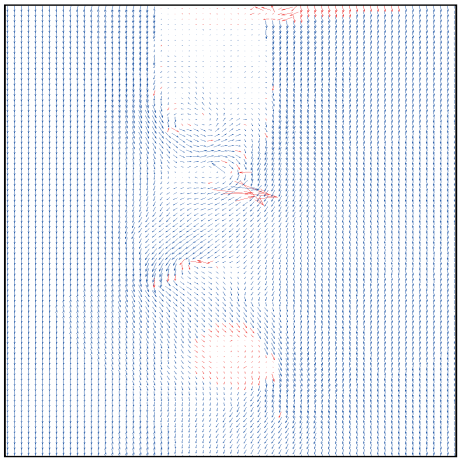

(b) Vector fields after applying the peak validation (398 rejected vectors).

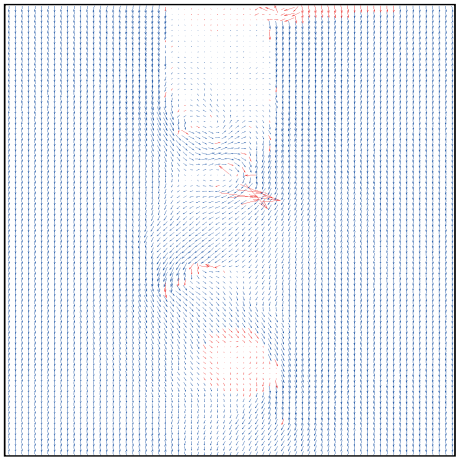

(c) Vector fields after applying the universal outlier detection (441 rejected vectors).

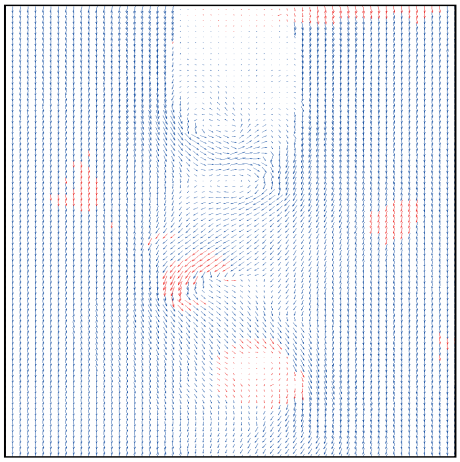

(d) Vector fields after applying the N-sigma validation (731 rejected vectors).

Figure 3–13: Successive applications of the validation methods: the total number of vectors is 16384.

assumed to be isolated, their neighbours are valid and the missing displacement can be computed by:

$$u_{i,j} = \frac{1}{2}(u_{i-1,j} + u_{i+1,j}) \text{ and } v_{i,j} = \frac{1}{2}(v_{i,j-1} + v_{i,j+1}), \tag{3.15}$$

where i and j are the indices of the missing vector. This procedure can be rendered more precise if additional neighbours are taken into account.

An alternate method is the Thin Plate Splines (TPS) used in the present work and described by Bookstein [6]. This method is based on the construction of a surface according to the value of the valid vectors. Thus, the missing vector can be interpolate on this surface. With this method, one operation per quantity is required, i.e. two for the two-dimensional velocity field.

3.5 Accuracy of a PIV measurement

When performing a PIV measurement, the errors sources can be classified into three groups: 1) inaccuracies in the positioning of the laser, camera and calibration target, 2) error associated with the time delay between laser pulses, and 3) errors in the computation of the displacement by the cross-correlation. The positioning error depends on the precision of the experimental apparatus, notably during the calibration. To minimize this error, motorized traversing mechanisms were used to move the camera, laser and calibration target. In this work, the largest component of this error stems from the alignment of the laser, which was done using special pins glued to the calibration target (see Fig. 4–5a), and limited by human accuracy, estimated to be within 1 mm. However, the approach used herein ensures that the perpendicularity between the laser sheet and the camera axis is never greater than 0.6°, such

that the error from the normal component velocity is negligible. The error associated with the time delay depends on the electronics used, which is less than 12.5 ns and corresponds to 0.12 % of the minimum time between pulses of 10 μs. The error in the computation of particle displacements depends on multiple parameters. Adrian and Westerweel [3] compiled a list of relevant factors that includes the tracer dynamics, the image mapping, the interrogation computation, the spatial resolution, the vector placement within the interrogation window, the flow kinematics, the sampling error, and the computation of the velocity derivatives. However the main limitation is the camera resolution (which is estimated to be 0.1 pixels [35], using subpixel refinement techniques), so that other sources of errors can be considered negligible. Given that the effects of camera resolution are i) the most significant source of error, and ii) dependent on the flow in each region in which measurements are performed, this error will be computed and specified for each measurement in the Results chapter, using:

$$\eta_v = \frac{\eta_{\Delta x}}{\Delta t}, \tag{3.16}$$

where $\eta_{\Delta x}$ is the error made on the displacement and Δt is the time interval between laser pluses.

Chapter 4
Experimental facilities

4.1 The scale model

As the access required to perform flow measurements on actual hydrogenerators is quite limited, a scale model was designed and built, based on an existing hydrogenerator in service at Hydro-Québec (Beauharnois). As described in Toussaint *et al.* [43], the scale model is a simplified version of a prototype that includes all main ventilation components, but excludes any active electromagnetic parts. As depicted in Fig. 4–1, the rotor spider arm acts as a pump that first drives the flow through the rotor rim and fan blades, then through the air gap, the stator, and finally the stator frame. Many components of the scale model are made of transparent material to provide optical access for the PIV measurements. Major simplifications in this scale model include the omission of the coolers and the use of a slotted cylindrical transparent plate as the stator, allowing measurements in the air gap and interpole regions. In the current study,"the cooler exit" region thus represents the space where the cooler would have been placed in a real hydrogenerator. The main characteristics of the scale model are listed in Table 4–1.

Although the overall size is scaled down, the dimensions of key components such as the air gap, rim ducts and stator ducts are the same as the prototype. Moreover, to preserve dynamic similarity between the model and the prototype, the rotational

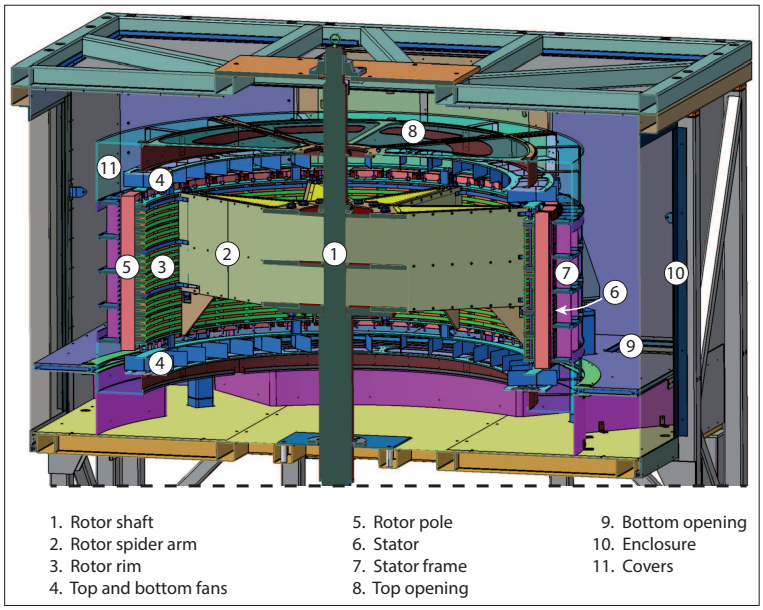

Figure 4–1: Schematic of the scale model, from [43].

velocity was increased (i.e., to keep the same Reynolds number (Re) based on the rotor radius):

$$\mathrm{Re} = \left[\frac{\rho(\omega_m r_m)e}{\mu}\right]_{model} = \left[\frac{\rho(\omega_r r_r)e}{\mu}\right]_{real}, \tag{4.1}$$

where ρ is the air density, ω_m and ω_r are the respective angular velocities of the model and of the real generator, r_m and r_r are the respective radii of the model and of the real generator, e is the air gap thickness, and μ is the dynamic viscosity of air.

Considering that the fluid characteristics primarily depend on the temperature, which is roughly the same in the model and the real generator ($\approx 45°\mathrm{C}$), equation 4.1 can be simplified into:

Table 4–1: Characteristics of the scale model, from ref.[43].

Rotor diameter	2.27 m
Rotor height	1.06 m
Number of rotor ducts	36×23
Dimensions of rotor ducts	23×12.7 mm^2
Number of poles	36
Stator inner diameter	2.3 m
Stator thickness	4.76 mm
Stator height	0.73 m
Number of stator ducts	72×29
Dimensions of stator ducts	43×6 mm^2
Number of radiator openings	4
Enclosure volume	$3.2 \times 3.2 \times 1.8$ m^3

$$\frac{\omega_m}{\omega_r} = \frac{r_r}{r_m} = 4. \tag{4.2}$$

Since the real generator at the Beauharnois plant rotates at 94.7 RPM, the scale model should therefore have a rotational velocity of 379 RPM to maintain the dynamic similarity. Although the model has been designed to operate up to a speed of 500 RPM, the series of measurements will be performed at a speed of 300 RPM to limit mechanical stresses in the scale model. As the main objective of this PIV campaign is to validate a numerical model, the simulations are also run at 300 RPM and the comparison will be made at this rotational speed.

4.2 PIV setup

A standard two-dimensional, two-component Dantec PIV system was used with DynamicStudio v4.10 software for the post-processing of the acquired data. The laser used for the measurements herein is a Nd:YAG double cavity (Solo PIV 200XT-532 nm, 15 Hz, 200 mJ). The camera is a FlowSense 4M Mk2 with a 60 mm or 105 mm lens, and a 532 nm band-pass filter. All non transparent components of the scale model were painted black to avoid laser reflections.

4.3 Seeding

Seeding of the flow in a model of this size is quite challenging since the oil droplet density needs to be uniform and sufficiently dense in the measurement area without perturbing the flow. A Laskin nozzle [24] was used to generate the droplets and the apparatus is shown in Fig. 4–2a. This system consists of four tubes submerged in canola oil that inject air at high pressure. The oil droplets are then convected to the measurement region using a piping system and a distributor, shown in Fig. 4–2b. The droplet density can be adjusted by regulating the air pressure into the four tubes, and a secondary air inlet is used to adjust the droplet flow rate. With this setup, around 100 particles per interrogation window were obtained, a good comprise between sufficient density and minimization of the particles superposition. To find the optimal seeding locations, preliminary tests were performed in which the oil droplets, invisible to the naked eye, were replaced by smoke injected by an apparatus developed for this purpose, as illustrated in Fig. 4–3. Observation of the smoke (either directly or using a GoPro® camera) was made to determine the best

locations to inject the oil droplets for the PIV measurements. Each measurement required a different seeding location.

(a) Laskin nozzle

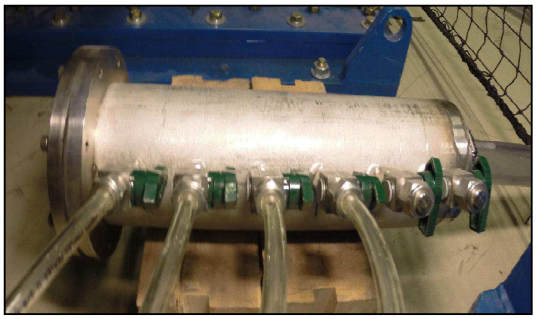

(b) Distributor

Figure 4–2: Oil seeding devices.

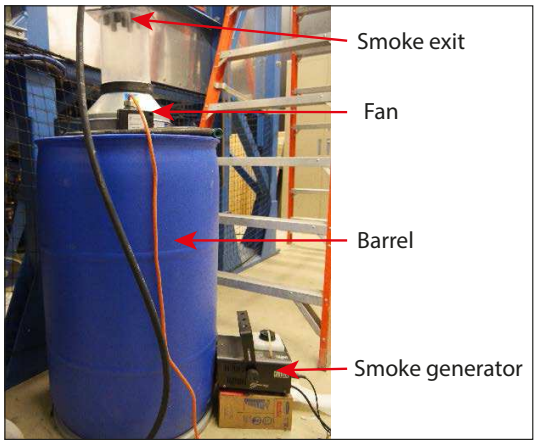

Figure 4–3: Home-made device to increase the smoke flow rate.

4.4 Mechanical supports

4.4.1 Laser and camera

The above-mentioned PIV system uses one camera to measure two velocity components in a plane illuminated by the laser sheet. To avoid projection errors, the axis of the camera needs to be normal to the laser sheet. To ensure this, a calibration target was employed for all measurement locations to align the optical equipment. To facilitate the motion of both the camera and the laser, a support with guiding rails (shown in Fig. 4–4) was built, which permitted numerous measurement configurations. In Fig. 4–4, the laser is placed on the upper support. The laser is connected to an extension arm that enables optical access through the top of the scale model, permitting laser light sheets in the x-z and y-z planes. This arm was designed to also support the camera. However, low frequency vibrations due to the operators displacements around the scaled model disturbed the camera's focus and rendered any measurements in this configuration impossible. Consequently, an additional support was built and placed on the scale model's structure to hold the camera, allowing a view of the x-y plane from above. The laser was not support by this arm during this experimental campaign and the mechanical support was enough rigid to avoid low frequency vibrations and detached from the scale model to avoid high frequency vibrations. Side access for the laser or the camera is also possible using the lower support. Finally, a special support was built for the pit opening measurements (not shown here).

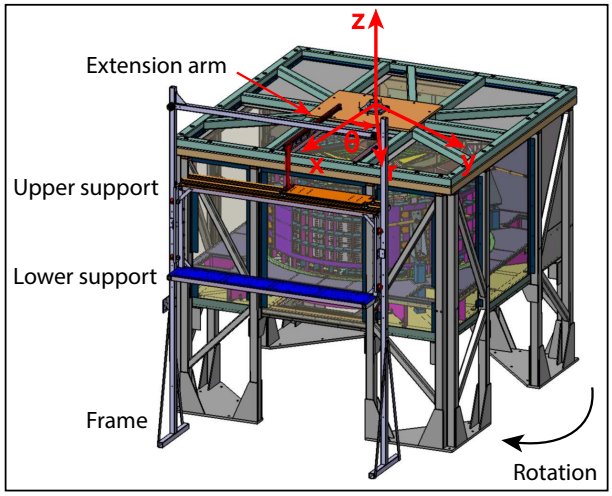

Figure 4–4: Support for the laser and the camera used in the majority of the measurements.

4.4.2 Calibration target

A PIV system requires calibration to convert pixels to physical dimensions. This step is critical and the target must be positioned with high accuracy to align both the laser and the camera. For each measurement region, a specific apparatus was made to insert the calibration target inside the scale model. To align the laser with the target, pins on the target were painted with a special paint that reflects the laser light at a different wavelength while absorbing most of its energy. This paint allows the user to see the laser sheet while wearing protective glasses so as to be able to safely align the laser. The calibration target, its support, and the special laser alignment pins are shown in Fig. 4–5 for two different measurements locations. The target itself is made of black dots on a white background. A bigger central dot defines the origin and four smaller dots are used to determine the orientations of the two axes.

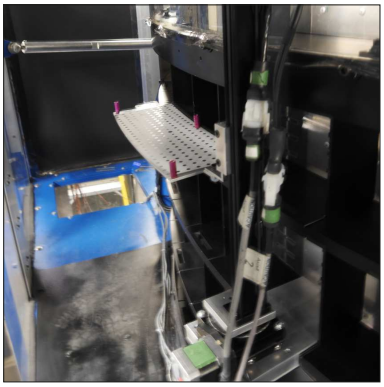

(a) For the cooler exit.

(b) For the air gap and interpole.

Figure 4–5: Calibration targets and supports.

Chapter 5
PIV results

In the present work, PIV measurements were made to determine the air velocities through the pit opening, between the cooler exit and the enclosure wall, at the cooler exit, in the cover region, in the air gap, and in the interpole region. The acquired data are furthermore compared with the CFD results. For all the results, the same coordinate system orientation has been used and is shown in Fig. 5–1. The origin is defined for each case at a fixed location in the scale model. All the x-y and r-θ planes results are viewed from the top, thus the scale model is rotating clockwise.

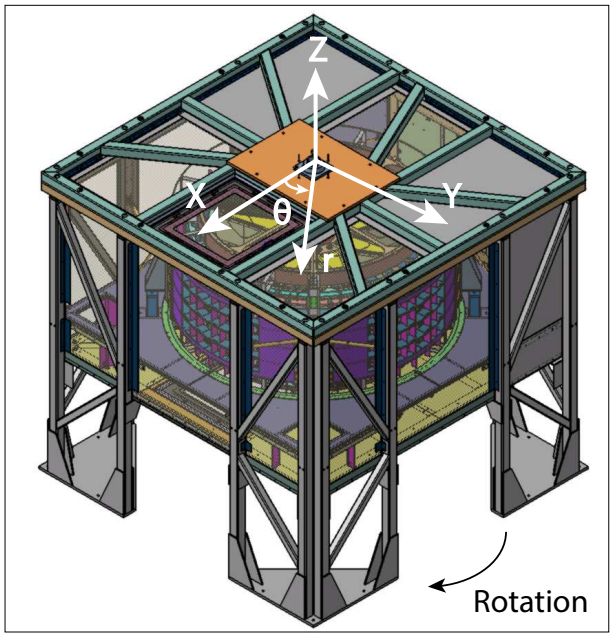

Figure 5–1: Coordinate system employed in the scale model.

During the course of the measurements, the operating temperature varied between 35°C and 40°C, due to windage losses. Thus, a mean temperature of 37°C has been chosen in the calculations. For the CFD, the simulation was run with an air temperature of 45°C, which corresponds to the equilibrium temperature in the scale model. A difference between these two temperatures was tolerated so as to be able to make measurements without having to wait approximately 6 hours for the apparatus to reach its equilibrium temperature. The air densities, used in all mass flow rate computations, are listed in Table 5–1.

Table 5–1: Temperature and density of the air in the scale model.

	PIV	CFD
Temperature (°C)	37	45
Air density (kg/m^3)	1.124	1.096

As the computation method is based on a statistical approach, a part of the velocity vectors are false. They are detected by the validation process. For each measurement, the velocity map can be divided into two parts: the internal and the external area. In the external part (outside of the flow or reflexions), the velocity vector is impossible to compute. There are represented by a blank area in the final result. In the internal area, the spurious vectors represent less than 2.5%, otherwise the vector is consider in the external area.

The details of the parameters used for each measurements are summarized in Appendix B.

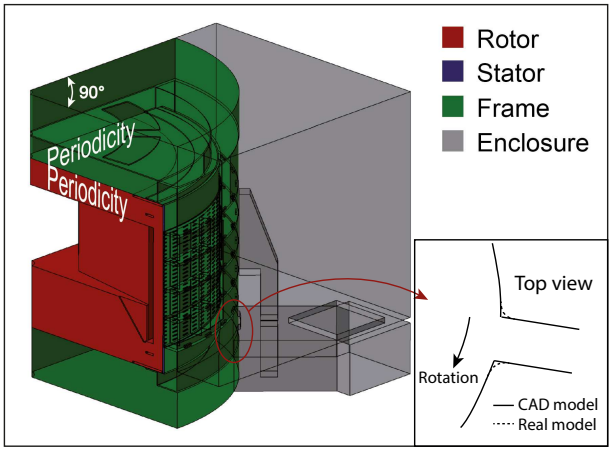

Figure 5–2: 3D computational domain.

5.1 CFD simulations

All the measurements have been compared with CFD results that were previously obtained by Toussaint *et al.* [43]. The three-dimensional computational domain used for the CFD simulations is shown in Fig. 5–2, which represents a 90° section of the scale model, to take advantage of the geometrical periodicity. The entire ventilation circuit was modeled and consequently no inlet or outlet boundary conditions were required (i.e., the mass flow rate of air is automatically computed). The rotor speed was set to 300 RPM, and the air properties were evaluated at 45°C, to be consistent with the experimental conditions.

Steady-state simulations were run with a commercial code (ANSYS-CFX) and the rotor-stator interface (RSI) was modeled using the MFR-MP (multiple frame of reference-mixing plane) interface option. With this approach, the rotation of a domain is taken into account by adding the centrifugal and Coriolis forces to the

momentum equations. Moreover, the velocity and pressure fields are circumferentially averaged before they are passed to the adjacent domain to obtain an average representation of all relative angular rotor positions with respect to the stator.

The hexahedral mesh consists of approximately 8.6×10^7 elements with 2.3×10^7 in the rotor domain and 6.3×10^7 in the static domain. A mesh independence study was performed to evaluate the appropriate level of refinement. The CFD simulations of the scale model were carried out with a Reynolds Average Navier-Stokes (RANS) $k-\epsilon$ model that uses a wall function to model the flow in the boundary layer. For this turbulence model, the first mesh node must be in the lower end of the logarithmic region of the turbulent boundary layer (i.e., at $y^+ > 30$) [9]. For this reason, the mesh refinement near the walls was adjusted to have a value of y^+ between 30 and 60. More details about the simulations can be found in Toussaint *et al.* [43].

5.2 Pit opening

For this measurement, the origin of the coordinate system is placed at the corner nearest to the rotor, as shown in Fig. 5–3. In this region, the air velocities are quite low and the flow is pulsating. Consequently, the seeding must be close to the measurement region to have sufficient particles without disturbing the flow. For this reason, placing the injection points behind the post at the entrance of the pit opening (shown in blue in Fig. 5–3) was a good compromise between these two requirements.

5.2.1 Validation

In section 3.5, it was shown that the main source of error in a PIV measurement is due to the discretization by the camera's CCD sensor. By using a subpixel refinement technique, this error drops to 0.1 pixels. For this specific measurement, one pixel

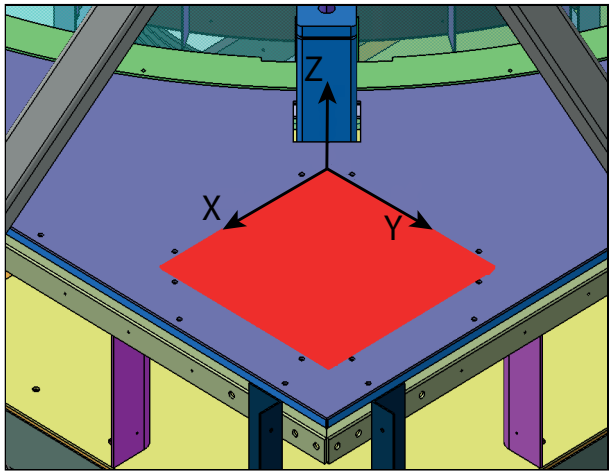

Figure 5–3: Measurement area and coordinate system in the pit opening.

represents 183 µm. As the time between pulses is equal to 450 µs, the accuracy of the velocity measurements is limited to 0.041 m/s (obtained from equation 3.16).

To check the repeatability of the measurements, one y-z plane located at $x =$ 88 mm was measured twice. The camera and the laser were moved and then repositioned at the original locations, using motorized axis, between the two experiments to further test the procedure. A line on the y-z plane, located at $z = 0$ mm was extracted and the axial velocity along this line is plotted in Fig. 5–4.

To compare these two profiles, the average axial velocity was computed for each measurement and a point-by-point comparison has been made using equation **??**.

Table 5–2: Repeatability of the measurements in the pit opening.

	Absolute difference (m/s)	Relative difference %
Average axial velocity	0.013	2.1
Point-by-point	0.030	7.4

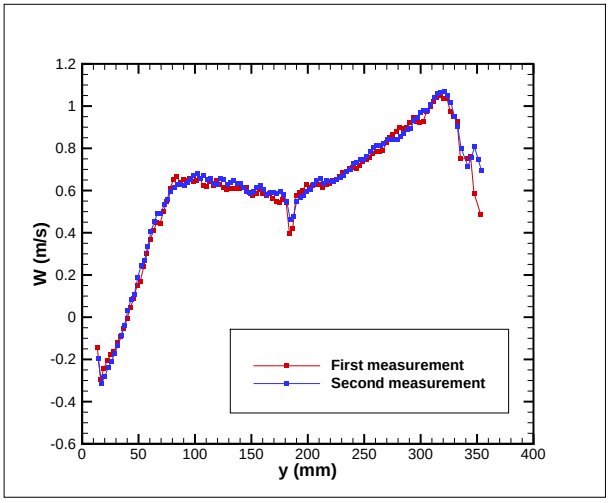

Figure 5–4: Test of repeatability: mean axial velocity at $x = 88$ mm and $z = 0$ mm.

As shown in Table 5–2, the observed differences in the mean axial velocity results and in the point-by-point comparison are below the precision of the measurement, thus validating the repeatability of the PIV measurements in the pit opening.

5.2.2 Results

Since the main objective here was to measure the flow rate across the pit opening, 10 x-z and 10 y-z planes were scanned with the laser sheet in the y- and x-directions, respectively. A linear interpolation was then performed to obtain a complete mapping of the axial velocity in the pit opening. The experimental results are shown on the left in Fig. 5–5, and were obtained by recording 2000 instantaneous velocity fields for each plane. However, some vectors were inevitably spurious, given that the correlation between the two frames is based on a statistical approach. A validation process was used to check each vector at every position and to reject spurious ones. As shown in Fig. 5–6, the number of remaining (i.e., non-spurious) vectors has to be higher than about 1500 to ensure converged data (at the given position). The convergence of

statistical quantities was ensured for each measured area given that the number of samples was flow-dependent. It was found that 2000 samples was largely sufficient for all measurements.

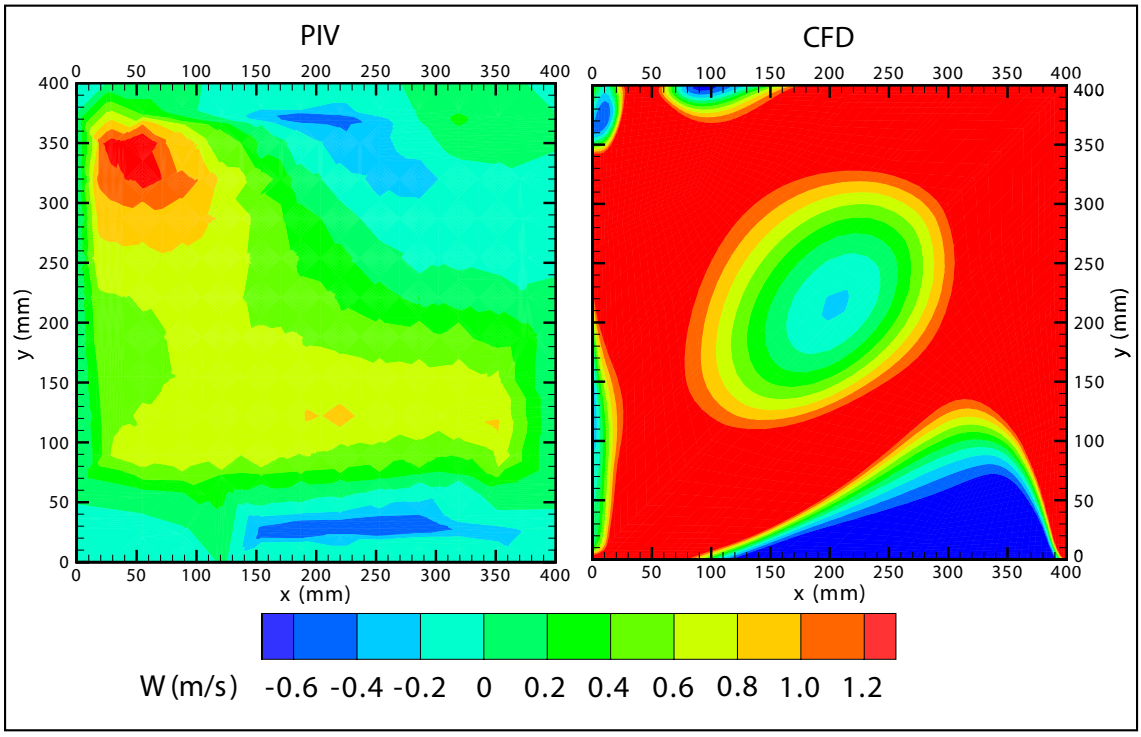

Figure 5–5: Contours of axial velocity through the pit opening.

The comparison between the PIV and CFD results in Fig. 5–5 shows some significant differences. This discrepancy is possibly due to a geometrical disparity in the entrance region of the pit opening between the scale model and the CAD version used for the CFD simulations. As shown in Fig. 4–1, the lower frame section consists of a cylindrical plate with four openings that allow the air to flow from the pit opening toward the rotor. In the scale model, the junction between the cylindrical plate and the pit duct has a 3 cm radius of curvature, whereas in the CAD model

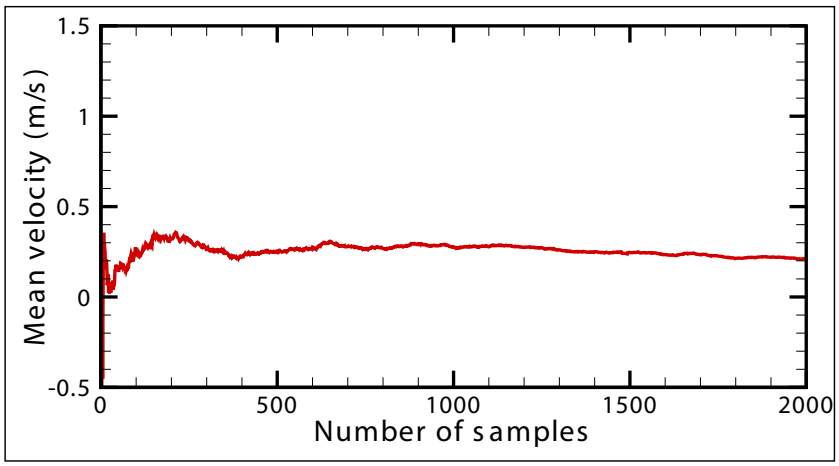

Figure 5–6: Convergence of the mean velocity in the pit opening ($x = 154$ mm, $y = 200$ mm).

this junction is sharp (see insert in Fig. 5–2). Due to the rotation of the rotor, the flow has a very high component of swirl and partially impinges on this junction. Since the junction is sharp in the CAD model, more air would enter in the pit duct and would flow towards the upper pit opening. Conversely, the rounded corner in the scale model might deflect a smaller part of the rotating flow toward the pit duct. Thus, a higher axial velocity and mass flow rate is observed through the pit opening for the CFD simulation, as summarized in Table 5–3.

Table 5–3: Mass flow rates and average axial velocities through the pit opening.

	PIV	CFD	Difference
Mass flow rate (kg/s)	0.056	0.261	366 %
Average axial velocity (m/s)	0.31	1.49	381 %

This hypothesis was partially validated by direct observation at the pit opening entrance, using smoke and a GoPro® camera. Moreover, it is interesting to mention

that the axial velocity in the pit opening in the actual prototype is negative (i.e., in the opposite direction compared to the scale model), since the flow is sucked from the enclosure toward the lower part of the rotor. The opposite flow direction between the scale model and prototype might be due once again to a higher radius of curvature at the junction between the pit duct and the lower cylindrical wall in the prototype, which may prevent the swirling flow from impinging on the side wall of the pit duct. This comparison demonstrates the large impact that small geometrical changes can have on the flow dynamics when they occur in a critical region, as the present one appears to be.

5.3 Space between the enclosure wall and the cooler exit

To have a global view of the flow in this area, three locations were considered: one plane at the center and one plane at each extremity of the cooler exit. For each location, the origin is centred at the cooler exit and on the floor, as shown in Fig. 5–7. Note that the rotation of the rotor (as viewed from above) is clockwise (i.e., from plane a) to plane c).

For these measurements, the seeding was done using two Loc-Line® tubes located just below the rotor spider arm. A high quantity of particles was needed and good mixing was achieved due to the highly swirling flow in this region. As it was impossible to paint the complete rotor, the laser pulses were synchronized with a section of the rotor painted to avoid reflections. Since the results must be independent of the rotor spider arm position, twenty different synchronizations of 100 images each were recorded to get an average value over the passage of a rotor spider arm.

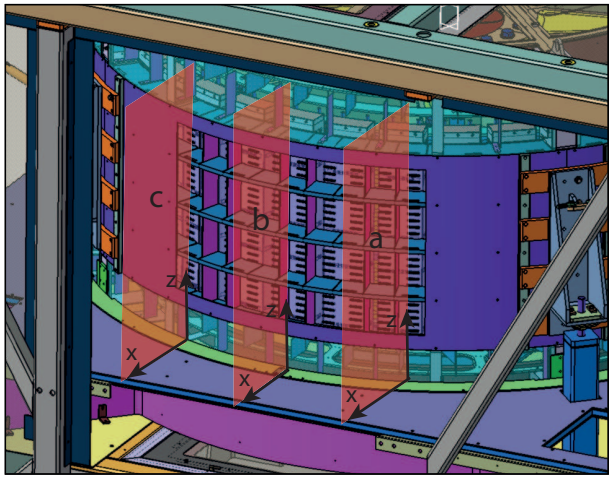

Figure 5–7: Measurement planes between the enclosure wall and the cooler exit.

5.3.1 Validation

In this configuration, one pixel represents between 234 µm and 375 µm, depending on the plane measured. As the time between laser pulses is equal to 200 µs, the accuracy of the velocity measurements is limited to 0.187 m/s (upper limit). Since the camera view is not sufficient to cover the entire height of the planes, two measurements have been made for each one. Moreover, the measurement has been repeated for the downstream plane with a third measurement at mid-height.

In Fig. 5–8, the axial velocity contours obtained from the first measurement are plotted as filled contours while the result from the second measurement is plotted as contours lines. One can see a good superposition of the two results. However, it was not possible to compute a quantitative comparison as that calculated for the pit opening results. As the camera was not at the same location for the two measurements, the undetected spurious points are not at the same positions. The spurious points are points with no valid mean velocity. These errors are mainly due

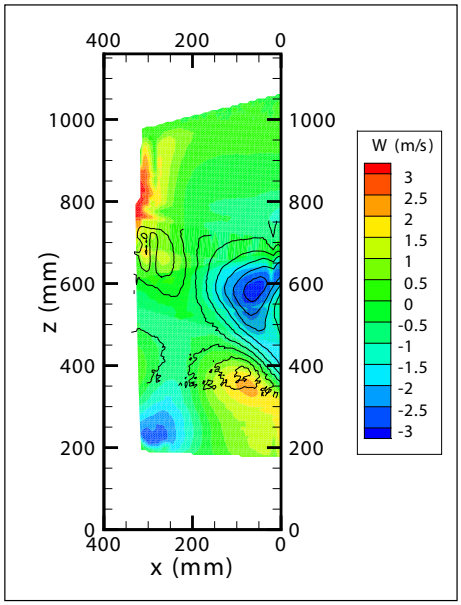

Figure 5–8: Test of repeatability: mean axial velocity in the downstream plane. (First measurement in filled contours, second in line contours.)

to the reflections. Even if there is a relatively low number of spurious points, around 500 out of a total of 16384 data points, the relative error is very large for these points, and it causes an overestimation of the mean relative error.

5.3.2 Results

The main goal of this measurement was to determine the axial flow distribution downstream of the cooler exit. The time averaged axial velocity contours in the three planes are plotted on the left side of Fig. 5–9. The blank areas are lack of measurements due to shadows resulting from laser obstructions (from the enclosure wall supports at the top and the bottom) or from camera obstructions (from the stator

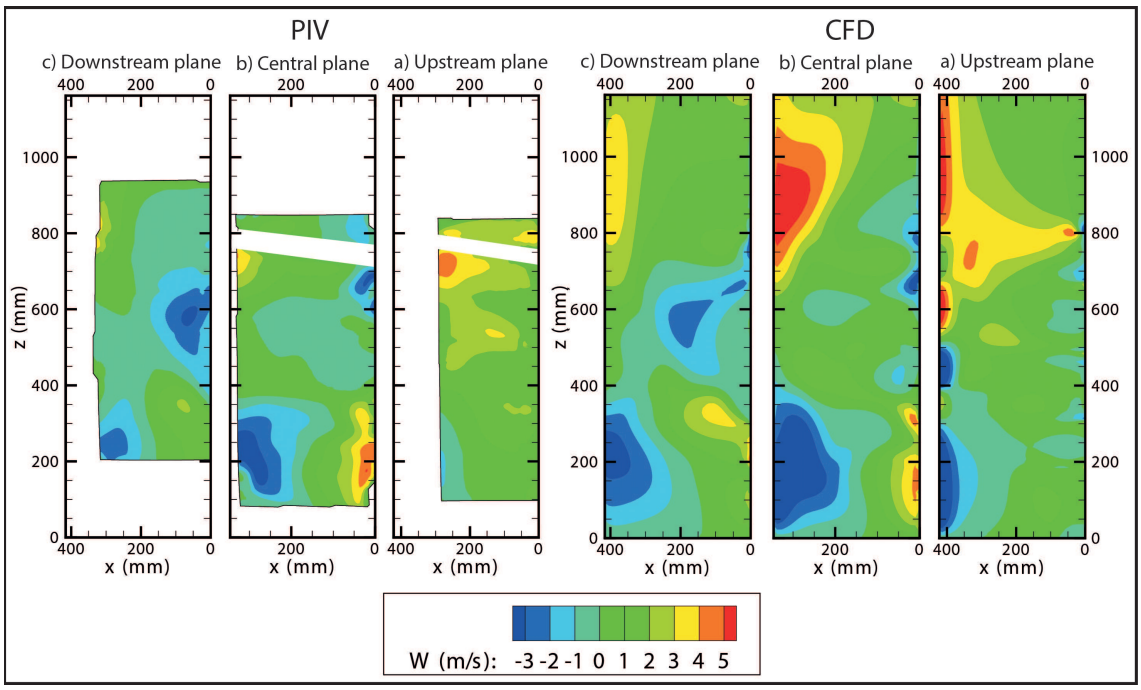

Figure 5–9: Contours of axial velocity in the space between the enclosure wall and the cooler exit.

support arm, located around $z = 750$ mm). The corresponding results obtained from CFD are presented on the right.

In all three planes, the air flow impinges on the enclosure wall (located at $x = 430$ mm) and is split into an upward and downward flow about the mid-height of the cooler exit (i.e., at $z = 500$ mm since the cooler exit is bounded by two covers at $z < 200$ mm and $z > 800$ mm). The axial velocities are found to be the highest in the central plane. This is due to the air that exits with higher velocities in the upstream zone of the cooler exit, (as will be discussed later with respect to Fig. 5–12) and that is then convected towards the central plane due to a circumferential flow component. In the downstream plane, the axial flow symmetry is less pronounced.

All these flow structures are present in both the PIV and the CFD results.

5.4 Cooler exit

To obtain a more quantitative comparison between the PIV and the CFD results, the mass flow rate was measured through the cooler exit. This region is of particular interest since almost the entire air flow passes through this location. To measure the radial velocity over the θ-z surface shown in Fig. 5–10, 20 r-θ planes were scanned over a distance of 570 mm in z with increments of 30 mm.

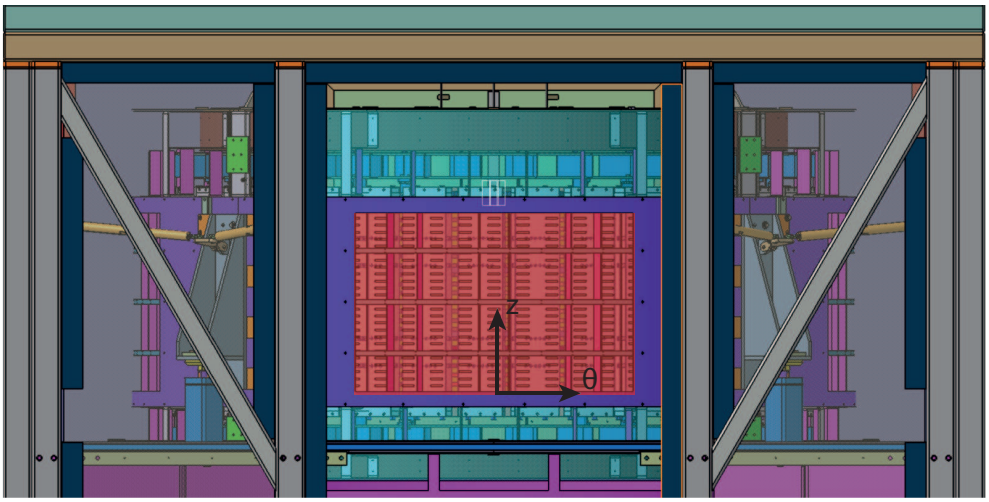

Figure 5–10: Cooler exit measurement area.

For these measurements, the same experimental procedure used for the space between the enclosure wall and the cooler exit was applied. Since the camera's field of view was not sufficient to cover the entire width of the cooler exit, each measurement in the r-θ plane had to be split in three separate regions.

5.4.1 Validation

In this region, one pixel represents 147 µm and the time interval between laser pulses varies between 80 µs and 120 µs, which limits the precision to 0.183 m/s (upper limit). The plane located at $z = 321$ mm has been measured twice with two different calibration targets and two positions of the camera. The radial velocity contours are superimposed in Fig. 5–11.

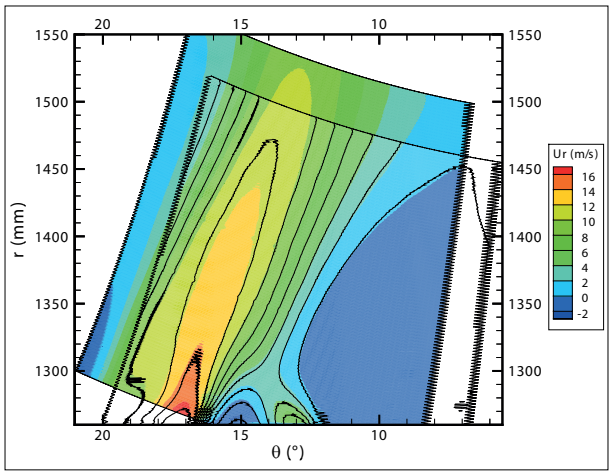

Figure 5–11: Repeatability test for the r-θ plane at $z = 321$ mm.

A quantitative comparison over the common area is presented in Table 5–4. The average axial velocity comparison is very good. However, the relative difference for the point-by-point comparison is moderate. This is explained by low velocity regions in the plane, increasing the relative error. Indeed, the absolute error remains of the same order of the maximal precision (0.183 m/s), validating the repeatability of the PIV measurements.

Table 5–4: Repeatability test in the cooler exit.

	Absolute difference (m/s)	Relative difference (%)
Average axial velocity	0.106	2.3
Point-by-point	0.234	22.5

5.4.2 Results

For each of the 60 r-θ measurements, a line at $r = 1270$ mm, (i.e., at a distance of 10 mm from the stator frame), was extracted and a linear interpolation was performed to obtain a radial velocity distribution across the whole cooler exit, as shown in Fig. 5–12.

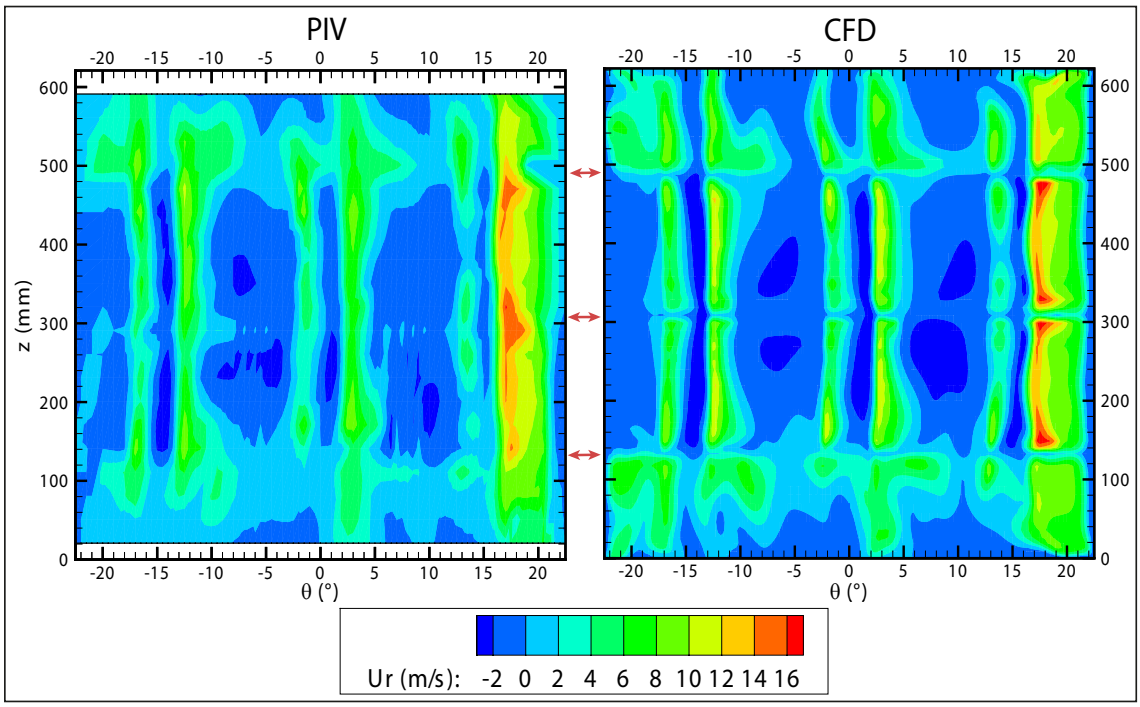

Figure 5–12: Contours of radial velocity through the cooler exit ($r = 1270$ mm).

At first, one observes that the flow distribution is uneven in the θ direction and the air mainly exits from the upstream region of the cooler opening. Indeed, all the flow exiting from the stator between two cooler openings is forced to turn clockwise inside the stator frame until it impinges on the vertical plates located at $\theta = 17.5°$ (visible in Fig. 5–7). The same phenomenon is observed, with a smaller intensity, on the plates of the stator frame, located at 12.5°, 2.5°, $-2.5°$, $-12.5°$ and $-17.5°$. To confirm this observation, the radial velocity contours have been plotted over a r-θ plane located at $z = 441$ mm (Fig. 5–13).

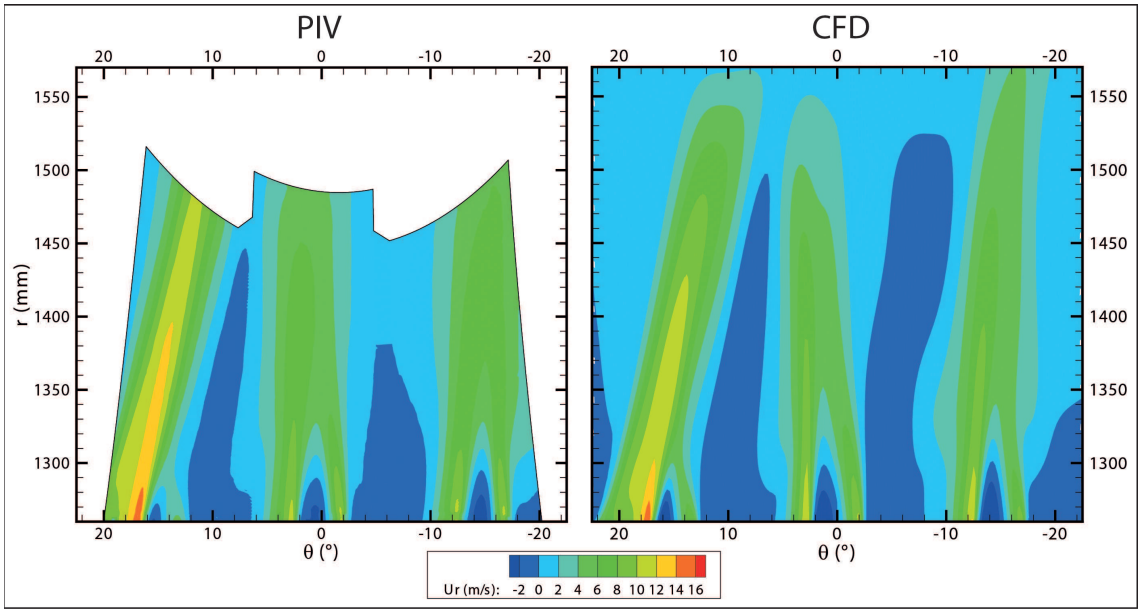

Figure 5–13: Radial velocity over a r-θ plane at $z = 441$ mm.

The six jets observed are clearly visible in both the PIV and the CFD results. Moreover, one can see that the two upstream jets are convected by a circumferential

component toward the central plane that was previously measured in the space between the enclosure wall and the cooler exit, explaining the higher velocities observed in Fig. 5–9.

In Fig. 5–12, two regions of higher velocity are observed at the top and at the bottom sections of the cooler exit due to an additional air flow coming from the covers through the rectangular opening in the frames shelves (circled in red in Fig. 5–15 of section 5.5). The r-θ plane at $z = 51$ mm is shown in Fig. 5–14. One observes that the six jets are still present, but their intensity is lower than the one observed in Fig. 5–13. This is due to the axial component of the flow. If the impinging flows on the vertical plate located at $\theta = 17.5°$ are similar, the one for the top and bottom regions are spread over the horizontal and the vertical directions. On the other hand, the flows in the central regions can only spread over the horizontal direction, which causes higher radial velocities.

These flow characteristics are present on both the PIV and CFD results, supporting the good accuracy of the simulation in this region. One can however notice in Fig. 5–12 a difference along three lines located at $z = 132$ mm, $z = 303$ mm and $z = 490$ mm (identified with three arrows in Fig. 5–12). This is due to the presence of three frame shelves in the stator (visible in Fig. 5–7). As no measurement was made at these specific locations, the linear interpolation could not detect the wake region downstream the shelves. Thus, a small overestimation of the flow rate is made by the interpolation of the PIV measurements. The mass flow rate is computed over the areas common to the PIV and CFD (i.e., 21 mm $< z <$ 591 mm). Table 5–5 shows a very good agreement between the numerical and the experimental values.

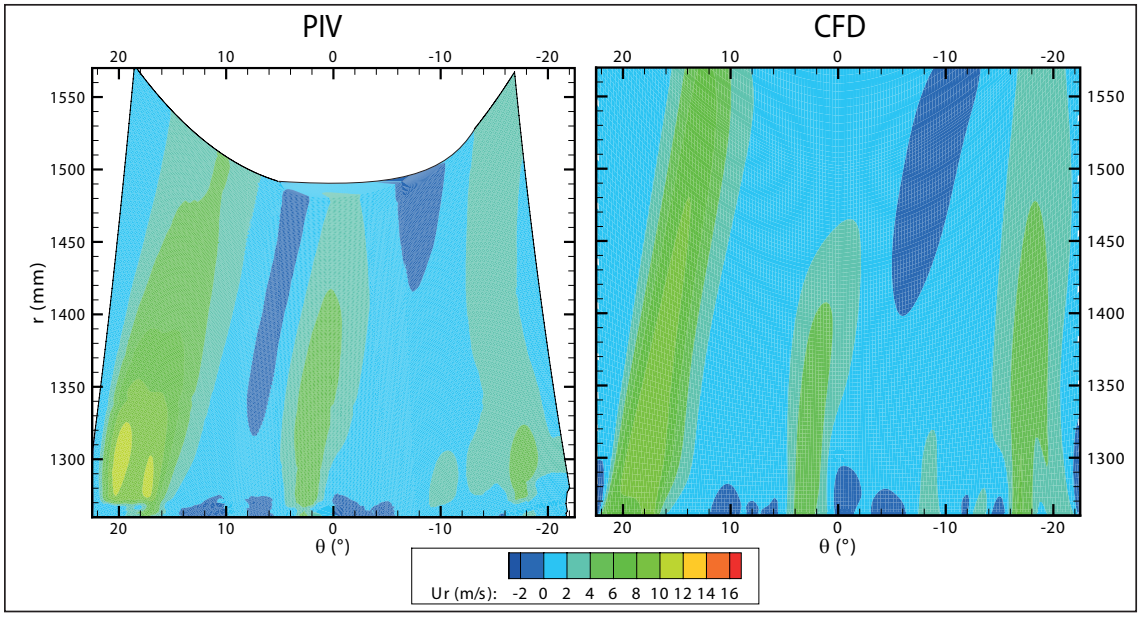

Figure 5–14: Radial velocity over a r-θ plane at $z = 51$ mm.

Table 5–5: Mass flow rate through the cooler exit.

	PIV	CFD	Difference
Mass flow rate (kg/s)	1.40	1.43	2.1 %
Average radial velocity (m/s)	2.02	2.10	4.0 %

5.5 Cover region

In the cover region, the choice was made to measure the circumferential velocity field over three r-z planes shown in Fig. 5–15. Their circumferential locations are $\theta = 0°$, $\theta = -2.5°$ and $\theta = +2.5°$, equally positioned between two planes symbolizing the end-windings. For this measurement, 12 r-θ planes were scanned at intervals of 20 mm in the z-direction from $z = 28$ mm to $z = 248$ mm. Since, the measured velocities were between 0 m/s and 15 m/s for all planes in the interval 28 mm $< z <$

148 mm, the selection of the time interval between laser pulses was more difficult. Indeed, use of a small time interval (to be capable of measuring the high velocities) increases the relative error for the low velocities. However, use of a larger time interval to increase the accuracy of the low velocities measurements causes a loss of particles in both interrogation windows, such that good quality measurements are no longer possible. Consequently, each plane was split into high and low velocity areas, measured independently with two different time intervals between laser pulses. Also note that the seeding was placed inside the cover to obtain a sufficient density of oil droplets.

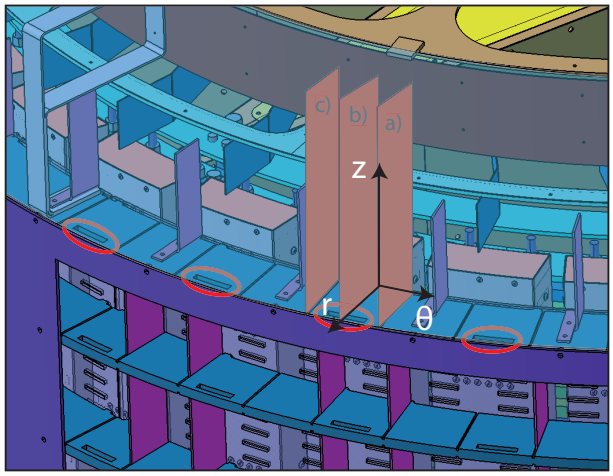

Figure 5–15: Measurement areas in the cover region.

5.5.1 Validation

For this measurement, one pixel represents 65 μm and the time interval between laser pulses varies between 20 μs and 120 μs, which limits the precision to 0.130 m/s. To validate the measurements, the r-θ plane at $z = 248$ mm was measured twice: at the beginning and at the end of the set of measurements. A quantitative comparison

is shown in Table 5–6 and the difference is less than the maximal precision, validating the repeatability of the results in the cover region.

Table 5–6: Repeatability test in the cover region at $z = 248$ mm.

	Absolute difference	Relative difference
Mean velocity (m/s)	0.01	0.3%
Point-by-point comparison	0.07	1.6%

5.5.2 Results

Before comparing the circumferential velocity contours in the r-z planes, the r-θ planes at $z = 88$ mm and $z = 248$ mm were chosen to qualitatively study the flow. To this end, a comparison of the vector plots between the PIV and CFD results is shown in Fig. 5–16. The plates representing the end-winding are plotted in grey at $\theta = \pm 5°$. The wake behind the upstream plate is clearly visible in Fig. 5–16a, where two asymmetric counter-rotating vortices are present since the main flow direction is not perpendicular to the plate.

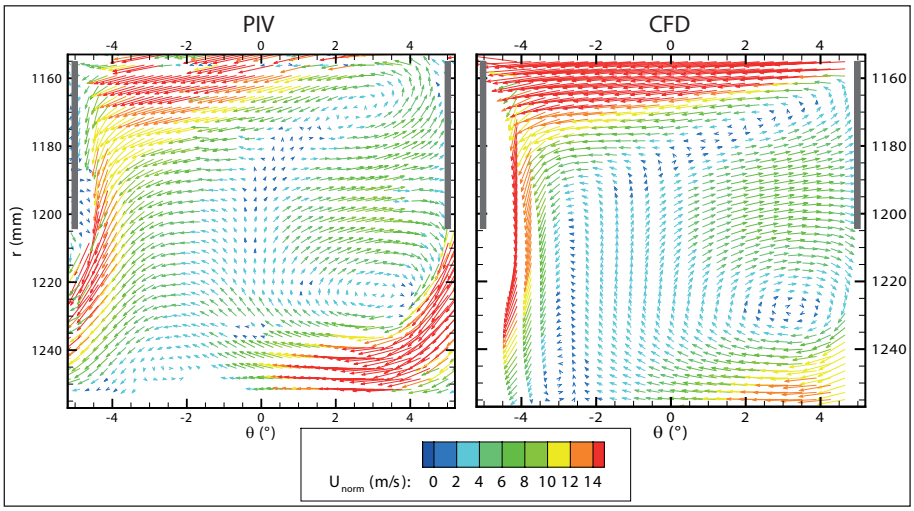

(a) $z = 88$ mm.

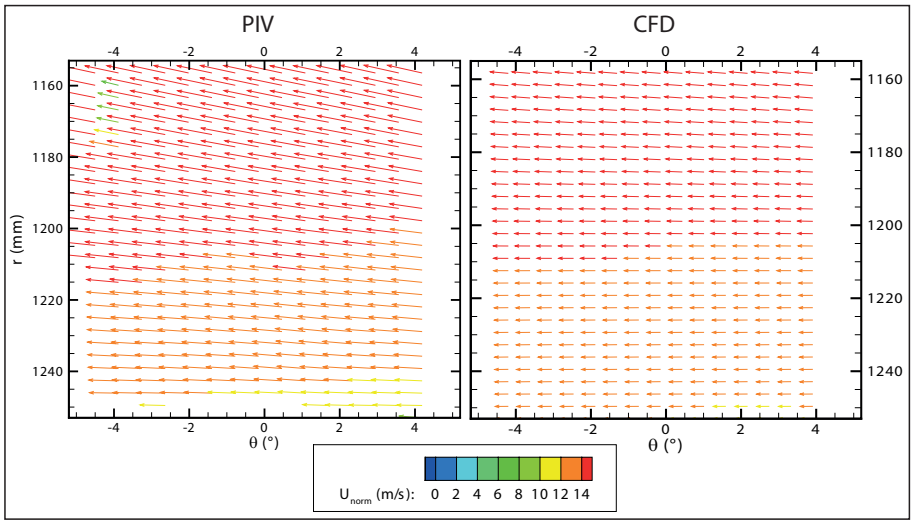

(b) $z = 248$ mm.

Figure 5–16: Velocity field in the cover region for two r-θ planes.

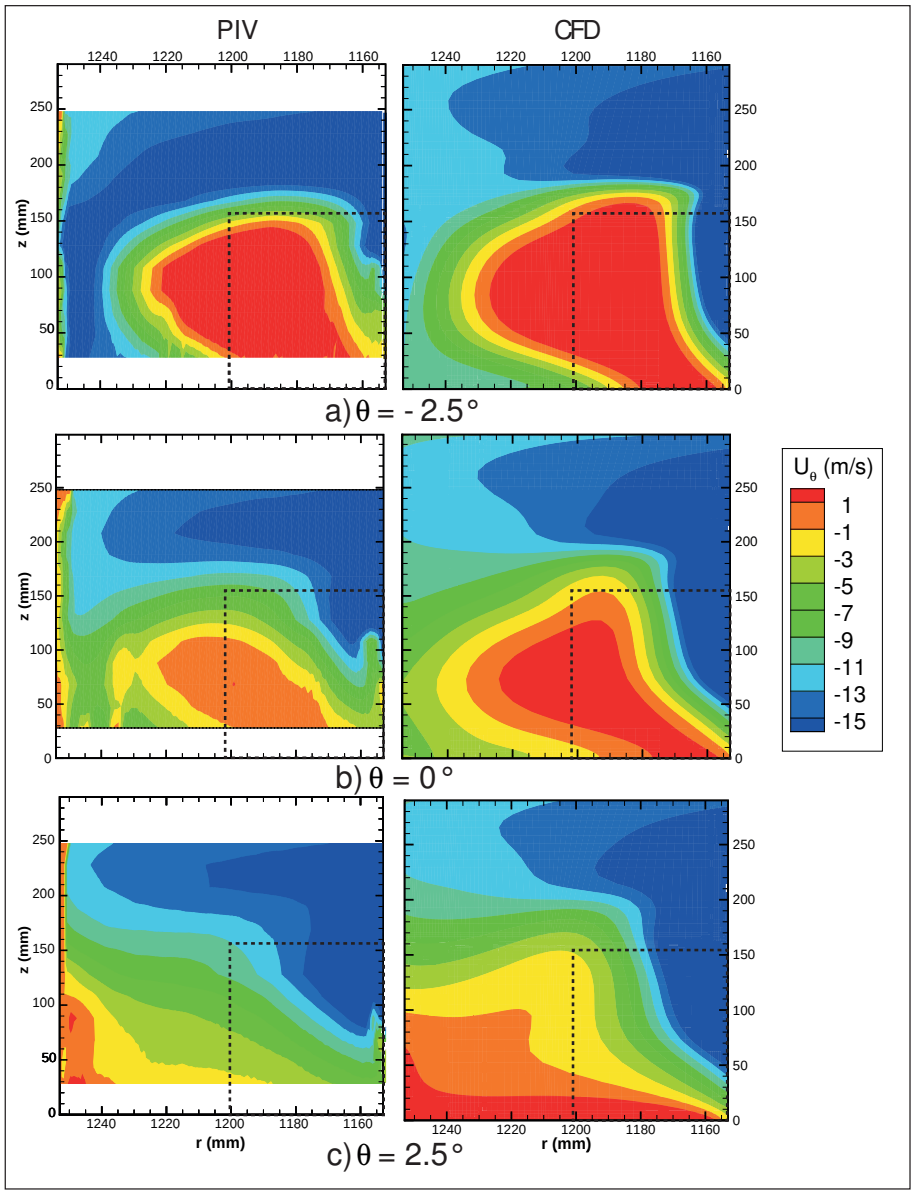

Figure 5–17: Circumferential velocity contours in the cover region. (Dashed lines represent the projected location of the end-winding plate).

In Fig. 5–16b, as there is no obstruction, the flow is almost uniquely circumferential, and it rotates at a velocity roughly half the one observed at the rotor tip. Qualitatively, the flow patterns are similar in the PIV and CFD results. From the flow field in r-θ planes located at different axial positions, the circumferential velocity over the r-z planes shown in Fig. 5–15 was obtained by interpolation and is plotted in Fig. 5–17. The dashed rectangle represents the projection of the stator end-winding plates, which are at $\theta = \pm 5°$.

Once again, the plate wake is visible at the three positions. Being convected downstream, it is increasingly offset with respect to the plate projection due to a radial velocity component in the main flow. In the upper region, for $z > 175$ mm, the flow has a strong rotational component, as observed in Fig. 5–16b. These flows patterns are present in both the experimental and simulation results.

To obtain a quantitative comparison, the mass flow rate over the surface area common both the CFD and the PIV measurements was computed for the three r-z planes and the results are shown in Table 5–7. Even though the agreement is not as good as for the cooler exit, the accuracy of the numerical simulation in this region is reasonable.

5.6 Air gap and interpole regions

In this region, 12 r-θ planes have been measured along the z-direction. The axial positions were imposed by the location of the stator ducts, used to insert the calibration target into the air gap. Thus, the minimal distance between two measurements planes is 24.3 mm. Moreover, three interpole regions were measured depending with their position being related to that of the spider arm. As shown in

Table 5–7: Mass flow rate in the cover region.

Position		PIV	CFD	Difference
$\theta = -2.5$ °	Mass flow rate (kg/s)	−0.248	−0.206	16.9 %
$\theta = 0$ °		−0.219	−0.197	10.0 %
$\theta = 2.5$ °		−0.200	−0.174	13 %
$\theta = -2.5$ °	Average circumf. velocity (m/s)	−9.65	−9.03	6.4 %
$\theta = 0$ °		−8.54	−7.85	11.2 %
$\theta = 2.5$ °		−7.88	−7.65	2.9 %

Fig. 5–18, the first one is in the middle of two spider arms and the others two are on the leading and the lagging sides of the spider arm. For each measurement, the laser sheet was placed in the center of the cooler opening width to minimize shadows.

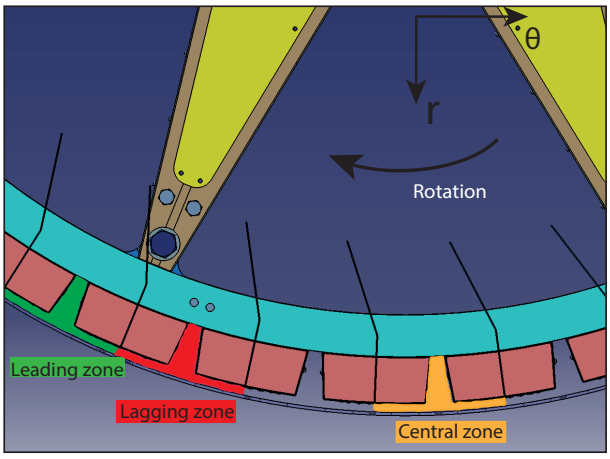

Figure 5–18: Measurement area in the air gap and interpole region (top view).

5.6.1 Validation

In this region, one pixel represents 65 µm and the time interval between laser pulses is between 10 µs and 15 µs which limits the precision to 0.650 m/s. This uncertainty is more significant than for the other regions, which can be explained by

the small size of the measured area (5×10 cm) and the short time interval between laser pulses due to the high velocities in the fixed reference frame. To validate the results, the measurement over the r-θ plane located at 133 mm from the bottom of the poles has been made twice, while completely stopping and restarting the scale model rotor between the two measurements. The results are presented in Fig. 5–19.

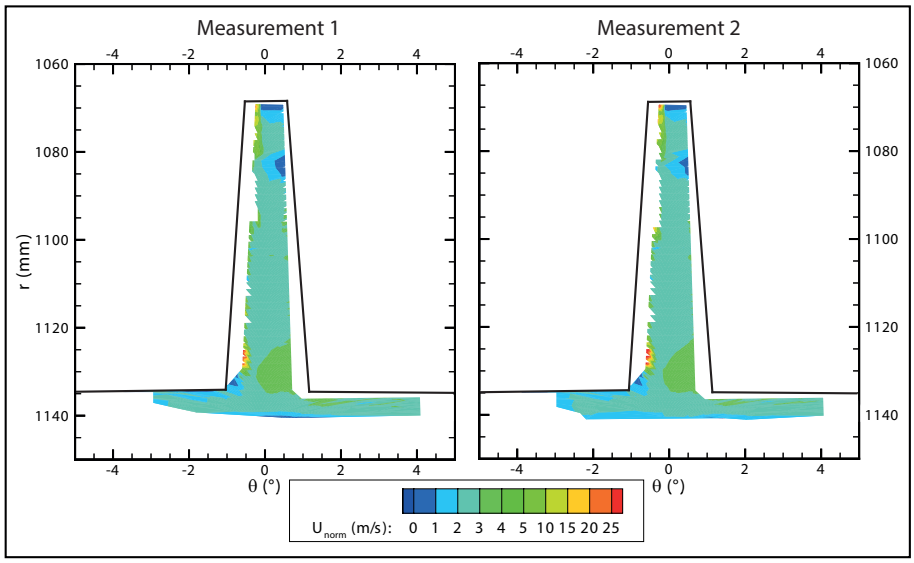

Figure 5–19: Repeatability test in the air gap and interpole region.

One can see that the planar velocity contours are very similar in both cases. To obtain a more quantitative comparison, the norm of the planar velocity has been compared over a common area of both measurement, and the results are shown in Table 5–8.

The average velocity comparison is very good and, even if the relative point-by-point difference is higher, the absolute difference remains under the maximum accuracy of the PIV in this region. Consequently, this test validates the repeatability of the PIV measurements in the air gap and interpole region.

Table 5–8: Repeatability test in the air gap and interpole region.

Average velocity (m/s)	0.006	0.2 %
Point-by-point	0.13	10.2 %

5.6.2 Results

The contours of Fig. 5–20 show the norm ($|\vec{U}| = \sqrt{u^2 + v^2}$) of the planar velocity in the rotating frame from both the PIV and the CFD results.

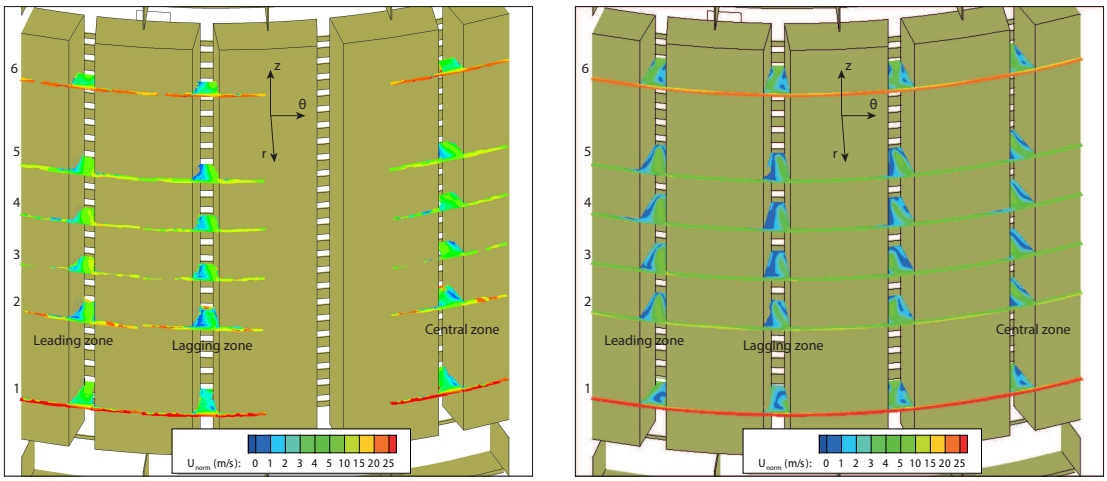

(a) PIV (b) CFD

Figure 5–20: Planar velocity contours in the air gap and interpole region.

One can first observe that the velocities in the air gap near the tops and bottoms of the poles (i.e., planes 1 and 6) are substantially higher. This is caused by the flow generated by the fans. In fact, the flow generated by the top and bottom radial fans mainly enters the interpole space and, only after penetrating a certain distance in the axial direction, exits through the air gap and goes around the pole face (see Fig. 5–21). Moreover, a strong vortex is present at each end of the interpole. This

vortex has a positive axial vorticity and thus convects the jets exiting from the rotor rim ducts toward the lagging side of the pole. More details on this flow are presented in [41].

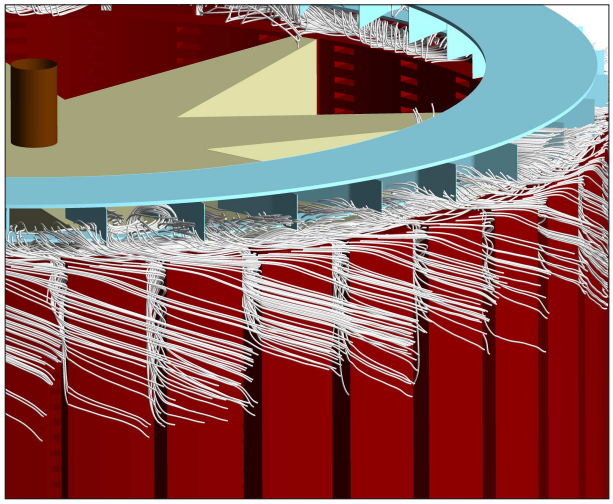

Figure 5–21: Streamlines of the mean flow generated by the fans, from [41].

Secondly, as expected, higher planar velocities are observed in the r-θ planes located in front of a rotor rim duct (i.e., planes 1, 2 and 6) compared to the planes located in front of the rotor rim (i.e., planes 3, 4 and 5). Finally, as shown in Fig. 5–22 for plane 4, the recirculation region in the interpole is closer to the pole trailing side for the leading and lagging zones, whereas it is closer to the pole leading side for the central zone.

The CFD results show that this difference comes from the velocity profile observed at the entrance of the rotor rim ducts. In fact, for the ducts located in the leading and lagging zone of the spider arm, the inlet velocity profile is relatively uniform and the main flow component is radial. On the other hand, for the ducts located in the central zone, the inlet velocity profile has a very strong tangential

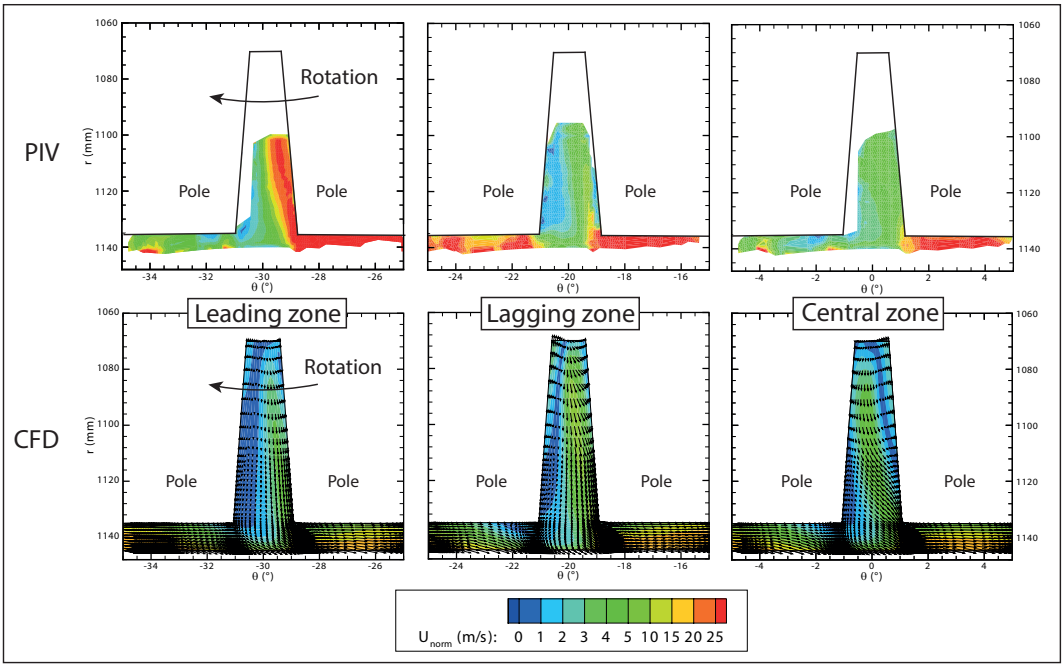

Figure 5–22: Planar velocity contours and vector plots in air gap and interpole region for plane 4.

component in the $+\theta$ direction that causes a large recirculation zone on the lagging side of the rotor rim duct. Therefore the flow impinges on the rim duct leading side and is then deflected in such a way that it exits from the rotor rim duct with a negative tangential velocity, thus creating a recirculation zone on the leading side of the interpole.

As the measurements were limited by the physical access to the air gap region, only 12 planes have been measured in the axial direction. Thus, an interpolation over an r-z plane in the air gap would not be accurate since, as shown in Fig. 5–20, there is strong non-uniformity in the z-direction due to the effects of the rotor ducts and the fans.

Chapter 6
Conclusions

6.1 General summary

Hydrogenerators are essential components in the production of electricity, converting mechanical energy into electrical energy. Even if their efficiency is around 95%, energy is nevertheless lost into heat. Thus, hydrogenerators have to be cooled by air circulation through their various components. However, this air flow is relatively unknown due to the geometrical complexity, rendering CFD simulations difficult and, due to the limited access, restricting measurements on operational hydrogenerator. For this reason, Hydro-Québec built a 1:4 scale model of a hydrogenerator without any electromagnetic components to study different aspects of the cooling, from the heat transfer at the poles faces, to the distribution of the mass flow rates of the cooling air. To measure precisely the air flow, PIV (Particle Image Velocimetry) was chosen.

PIV is an advanced experimental technique that allows the measurement of the instantaneous velocity field in a plane. Substantial effort was put into designing the PIV setup for the measurements on the scale model and, more specifically, building camera and laser supports, designing the calibration targets, and finding appropriate seeding locations. Several challenges were overcome to successfully implement the

PIV on the scale model, achieving measurements with a spatial resolution of one millimeter in a model several meters in size. Particle image velocimetry measurements in five regions of a scale model of a hydrogenerator were performed.

For the measurements in the pit opening, it was observed that differences between the real geometry of the scale model and the CAD version in the CFD simulation – initially deemed minor – can lead to significant variations in the fluid flow dynamics. In this particular case, it would be of interest to modify the pit geometry and rerun the CFD simulations to determine the sensitivity to such modifications and/or repeat the measurements with various geometries at the entrance of the pit opening.

The measurements and CFD simulations for the flow through the cooler exit and for the flow in cover region are in much better agreement than those of the flow through the pit opening, resulting in differences in mass flow rates of 2% and 13%, respectively. For the flow between the enclosure wall and the cooler exit, and for the flow in the air gap interpole region, the PIV measurements and the CFD simulations were qualitatively similar. This validation process gives confidence in the capability of CFD tools to correctly model such complex flows.

In a larger context, performing experimental measurements in the main flow regions of the scale model has improved our knowledge of the cooling in hydrogenerators. In particular, the flows in the various components are better understood (both qualitatively and quantitatively), and will provide useful insight that will help in the optimization of the cooling of hydrogenerators.

6.2 Further development

The main objective of the AUPALE project at Hydro-Québec is to improve the ventilation in hydrogenerators. Given the results of the PIV experiment carried out in the present work, a large amount of experimental data has been acquired and serves to validate the CFD results. Unfortunately, the PIV technique cannot be used to characterize the flow on a real hydrogenerator for practical reasons already described. However, the current PIV data will be used to determine the accuracy of simpler flow sensors that can be installed on actual machines.

The scale model geometry will be further modified in the future to test other ventilation configurations and PIV measurements will be repeated to determine the effect of geometrical changes on the flow dynamics. The PIV data will also serve to validate the numerical results for each tested configuration.

Appendix A
DynamicStudio software settings

Unless otherwise specified, the following settings in the DynamicStudio software were selected and applied to the images used to obtain the mean velocity field:

1. Adaptive Correlation
2. Vector Masking
3. Universal Outlier Detection
4. N-Sigma Validation
5. Vector Dewarping
6. Vector Statistics

Adaptive Correlation

In Fig. A–1a, the interrogation window is set to 32×32 pixels for the final interrogation area size to satisfy the usual compromise between spatial resolution and sufficient particles tracked. However, such a small size requires an equally small time interval between laser pulses. To catch more particles without decreasing the time interval, the adaptive correlation starts with an bigger interrogation window. The commonly accepted minimum for this initial size is 128×128 pixels, thus the number of refinement steps has to be 2 or more. Moreover, at each step, the interrogation window moves with the flow using the velocity computed at the previous step. Increasing the number of steps for each interrogation window size increases the percentage of particles that remains in the interrogation window. Usually, 2 steps for

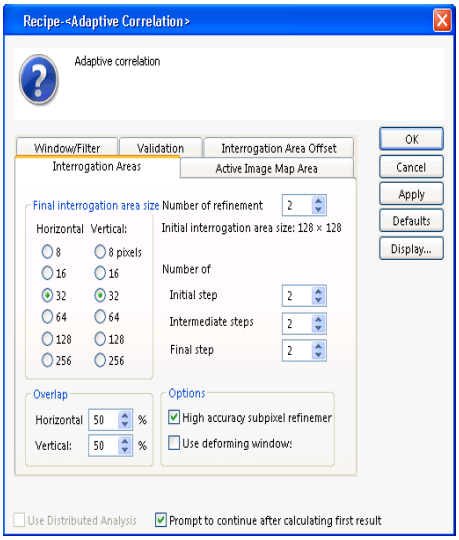

(a) Interrogation areas.

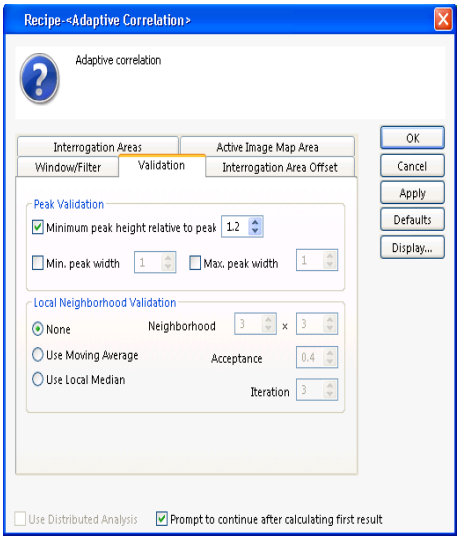

(b) Peak validation.

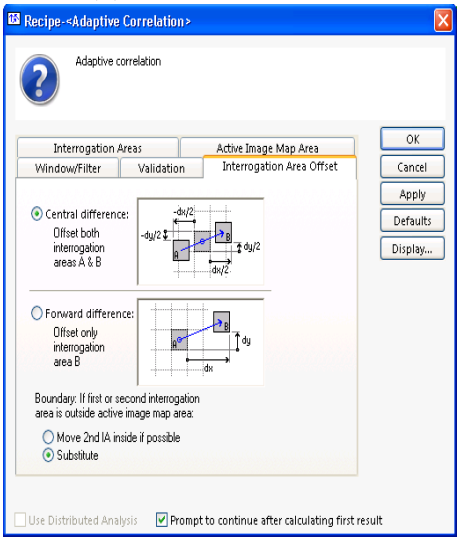

(c) Interrogation area offset.

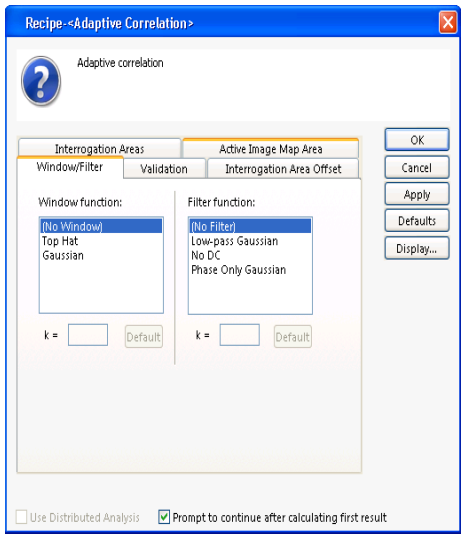

(d) Window and filter functions.

Figure A–1: Adaptive correlation settings.

each size is sufficient. High accuracy subpixel refinement is selected. (Its application was described in section 3.4.1). Finally, a 50% overlap in both the horizontal and vertical direction is chosen – a typical choice to improve the spatial resolution without reducing the size of the interrogation areas. In Fig. A–1b, the peak validation, as described in paragraph 3.4.2, is set to apply an initial filter to the result. However, the neighborhood validation is not applied at this step, as the neighbours have not been validated yet. In Fig. A–1c, the central difference scheme is selected so that the velocity vector is located at the center of the chosen interrogation window. At the borders of the measurement area, the vectors are substituted, according to the method described in paragraph 3.4.3. In Fig. A–1d, no window nor filter functions are selected given that the interrogation windows contains a moderately large number of pixels. Finally, in the "Active image map area" tab (not shown), the full image map is used to compute the vector field.

Vector Masking

In Fig. A–2, the user specifies the threshold percentage so that the mask becomes effective. This percentage depends on the mask: if it is very precise and carefully follows the contours of the unwanted object, this percentage must be low. However, in the case where the borders of the measurement area are not critical and small with respect to the measurement area, it is not necessary to define a precise mask and the percentage can be higher, around 50%, such a case, which correspond to the present one.

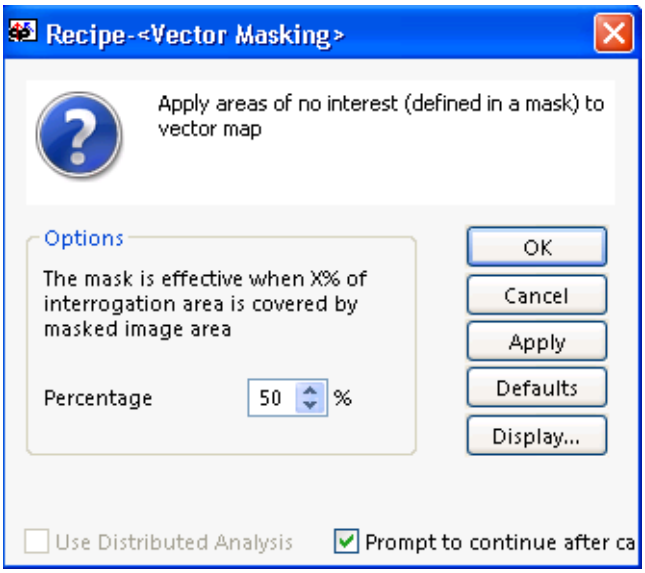

Figure A–2: Vector masking parameters.

Universal Outlier Detection

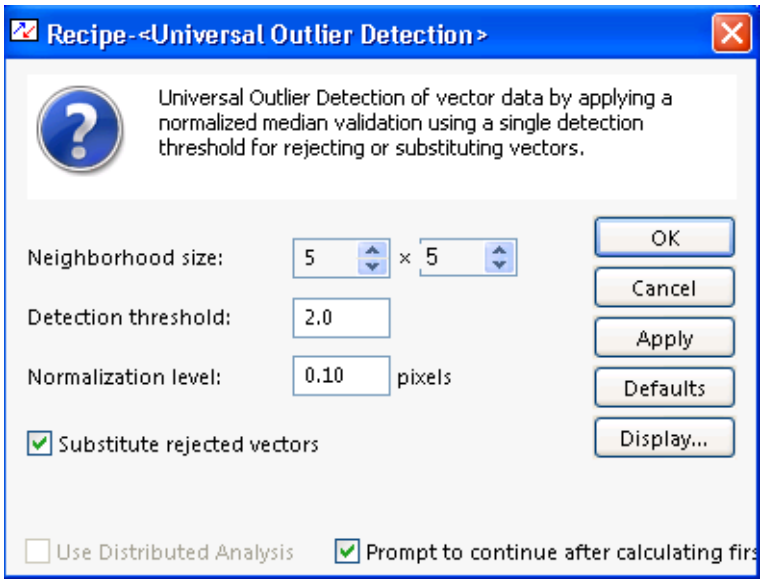

Figure A–3: Universal outlier detection parameters.

In Fig. A–3, the values advised by Westerweel and Scarano [46] are set for three parameters described in section 3.4.2 – a neighborhoud size of 5×5 pixels, a detection threshold of 2.0%, and a normalization level of 0.1 pixels

N-Sigma Validation

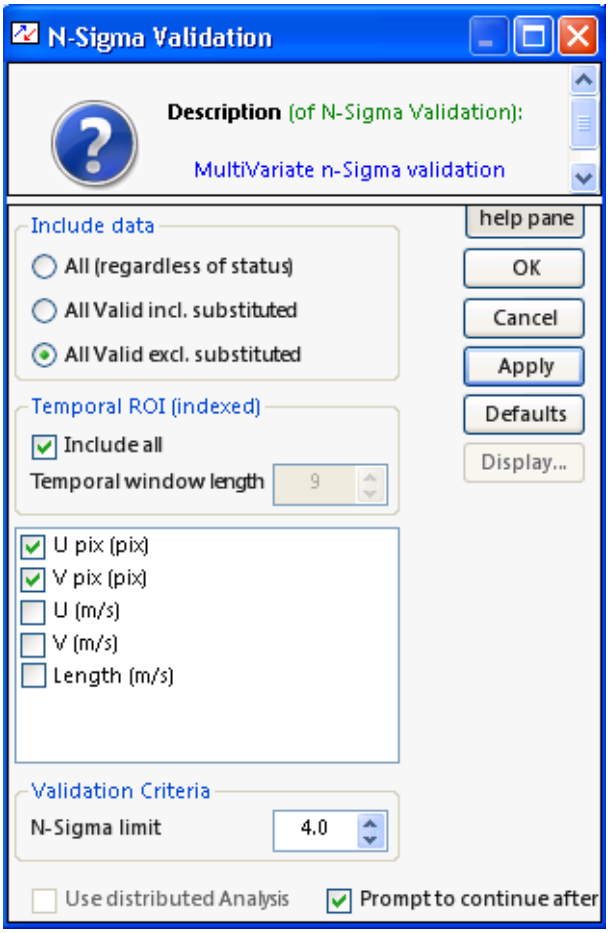

Figure A–4: N-sigma validation parameters.

In Fig. A–4, the validation is computed only for the remaining valid vectors after the universal outlier detection step. The software allows the user to select a specific time interval over which the validation is computed. As this is not required

in our case, the "Include all" option is selected. The N-sigma limit must fall between 4 and 6, depending on the variability of the flow. This value was adjusted for each measurement.

Vector Dewarping

At this step, the calibration is applied. To determine it, the "Image Model Fit" step computes a projection grid using a photograph of the calibration target, as shown in Fig. A–5. To check the quality of this calibration, one must look at the average retroprojection error, which must be lower than 0.5 pixels. More details on the calibration can be found in [4] (Hydro-Québec intern document).

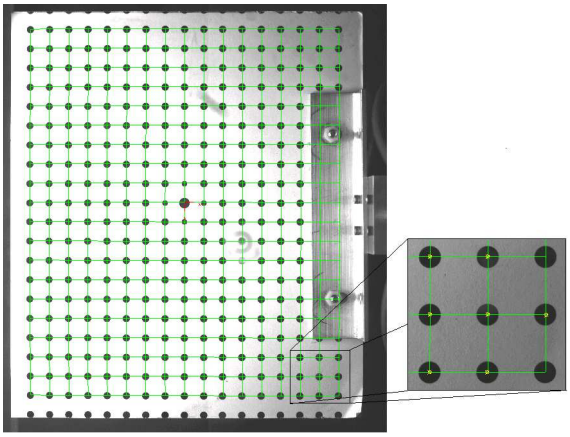

Figure A–5: Calibration target (dots) and imaging model fit (grid).

In Fig. A–6, the perpendicular direction and velocity are specified for the application of the calibration. As the calibration target is always placed in the measurement plane, Z is set to 0. On the other hand, the perpendicular velocity is unknown, thus $W = 0$ is chosen. The laser sheet and the axis of the camera are perpendicular to each other, to a very close approximation as discussed in section 3.5.

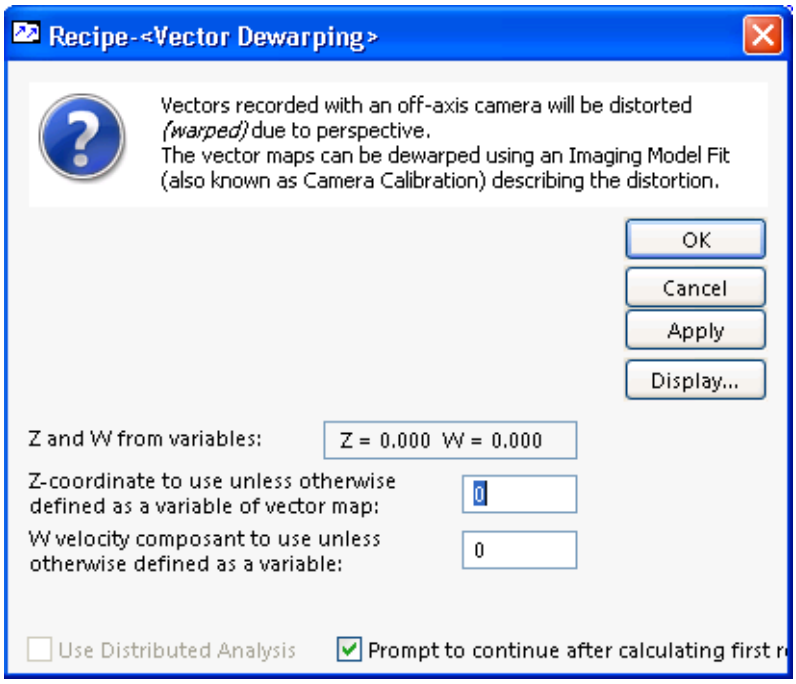

Figure A–6: Vector dewarping parameters.

Vector Statistics

To compute the vectors statistics, all the valid vectors, without the substituted ones are taken into account, as shown in Fig. A–7.

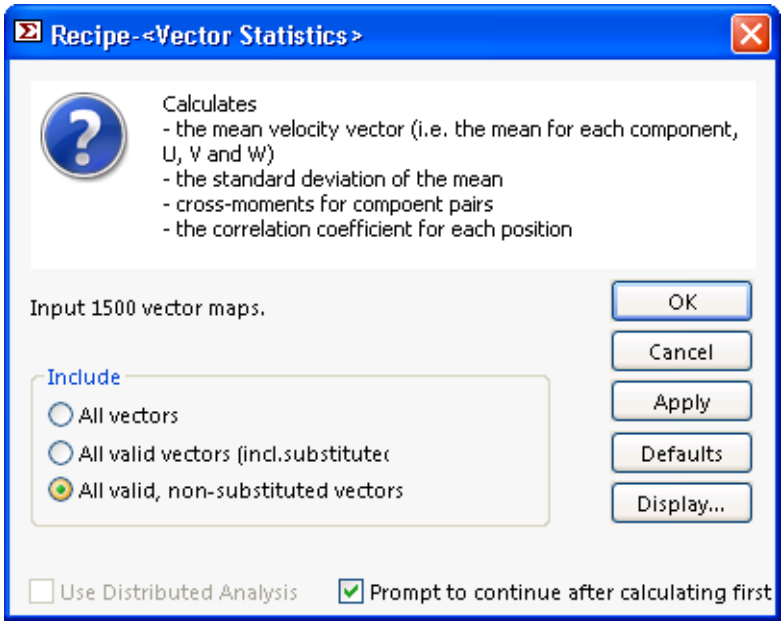

Figure A–7: Vector statistics parameters.

Appendix B
PIV parameters

For all measurements, the same materials was used. The laser sheet thickness is around 2 mm and was re-ajusted before each measurement. The camera aperture was 8.0 and the lens focal length was 65 mm. The maximum particle displacement was always under 8 pixels, and checked for each measurement. However, because of the presence of a large velocity component perpendicular to the laser sheet, the average displacement was 4 pixels. For the air gap and interpole region, the camera lens was changed to have a focal length of 105 mm.

The average velocity is computed from 2000 samples for all measurements. However, the others parameters such as the time between laser pulses can vary depending on the measurement region. The following tables list all the parameters for each measurement location. The time between the two laser pulses is denoted "TBP" (The definition of this parameter was explained in Fig. 3–6.). Moreover, some measurements require synchronization with the rotor. For these locations, different relative positions of the rotor were chosen to obtain an average velocity over the rotor passage. Only the first trigger delays are tabulated. The increment is equal to 1250 μs (i.e., the time needed for a 2.25° rotation). Thus, the 20 synchronizations cover an angle of 45° (i.e., the angle between two spider arms). In Fig. B–1, the position of the painted section of the rotor at the start of the trigger signal is shown.

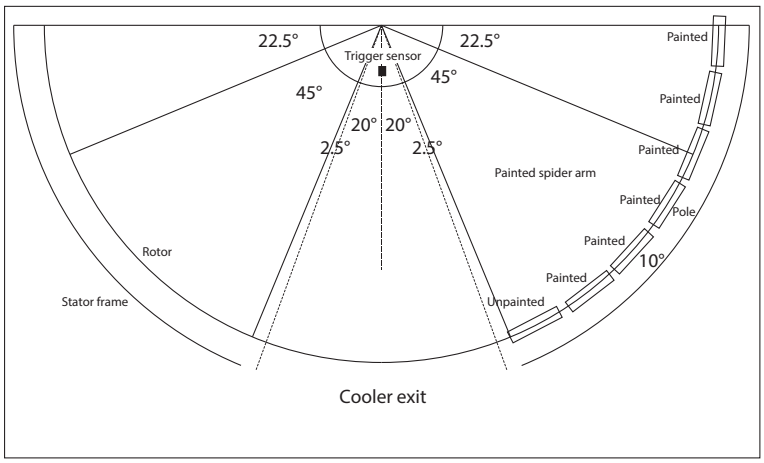

Figure B–1: Position of the painted section at the start of the trigger signal.

Pit Opening

In this region, 20 x-z and y-z planes were measured. There was no synchronization on the rotation (i.e. Trigger mode: Internal). The parameters are shown in Table B–1. Moreover, since the camera view angle was not large enough to cover the entire pit opening area, the x-z planes had to be split in two separate regions.

Table B–1: PIV parameters in the Pit Opening

x-z planes	y-position (mm)	56	89	122	155	188	221	254	287	320	353
	TBP (μs)	450	450	450	450	450	450	450	450	450	450
y-z planes	x-position (mm)	55	88	121	154	187	220	253	286	319	352
	TBP (μs)	450	450	450	450	450	450	450	450	450	450

Space between the enclosure wall and the cooler exit

For this region, three x-z planes were measured. Since the camera's field of view was not sufficient to cover the entire area, each measurement was split in two

separate regions. The parameters are summarized in Table B–2. Moreover, to avoid laser reflections, the measurements were synchronized with the passage of a section of the rotor that was painted black.

Table B–2: PIV parameters in the space between the enclosure wall and the cooler exit.

Plane	Height (mm)	TBP (μs)	First trigger delay (μs)
Upstream plane	341	200	9722.125
	661	200	9722.125
Central plane	361	200	20833.125
	680	200	20833.125
Downstream plane	456	200	31944.125
	806	200	31944.125

Cooler exit

To measure the radial velocity over the θ-z surface shown in Fig. 5–10, 20 r-θ planes were scanned over an extent of 570 mm in the z-direction in increments of 30 mm. Since the camera's field of view was too small to cover the entire width of the cooler exit, each measurement in the r-θ plane was split in three separate regions: the upstream, central and downstream zones. The synchronization was identical to the one used in the space between the enclosure wall and the cooler exit, but with a different initial trigger delay. The different parameters for the 60 measurements are given in Table B–3.

Table B–3: PIV parameters in the cooler exit.

N°	Height (mm)	θ position	TBP (μs)	First trigger delay (μs)
1	21	Upstream	120	13888.75
		Central	150	22222
		Downstream	160	30555.25
2	51	Upstream	100	13888.75
		Central	150	22222
		Downstream	140	30555.25
3	81	Upstream	100	13888.75
		Central	150	22222
		Downstream	130	30555.25
4	111	Upstream	100	13888.75
		Central	140	22222
		Downstream	130	30555.25
5	141	Upstream	80	13888.75
		Central	130	22222
		Downstream	120	30555.25
6	171	Upstream	80	13888.75
		Central	130	22222
		Downstream	120	30555.25
7	201	Upstream	80	13888.75
		Central	130	22222
		Downstream	110	30555.25
8	231	Upstream	80	13888.75
		Central	130	22222
		Downstream	120	30555.25
9	261	Upstream	80	13888.75
		Central	130	22222
		Downstream	120	30555.25

Continued on next page

N°	Height (mm)	θ position	TBP (µs)	First trigger delay (µs)
10	291	Upstream	90	13888.75
		Central	130	22222
		Downstream	140	30555.25
11	321	Upstream	80	13888.75
		Central	100	22222
		Downstream	90	30555.25
12	351	Upstream	80	13888.75
		Central	100	22222
		Downstream	90	30555.25
13	381	Upstream	80	13888.75
		Central	100	22222
		Downstream	90	30555.25
14	411	Upstream	80	13888.75
		Central	100	22222
		Downstream	90	30555.25
15	441	Upstream	80	13888.75
		Central	100	22222
		Downstream	100	30555.25
16	471	Upstream	80	13888.75
		Central	100	22222
		Downstream	100	30555.25
17	501	Upstream	80	13888.75
		Central	100	22222
		Downstream	110	30555.25
18	531	Upstream	80	13888.75
		Central	100	22222
		Downstream	110	30555.25

Continued on next page

N°	Height (mm)	θ position	TBP (μs)	First trigger delay (μs)
19	561	Upstream	80	13888.75
		Central	100	22222
		Downstream	120	30555.25
20	591	Upstream	90	13888.75
		Central	120	22222
		Downstream	130	30555.25

Cover region

In this region, 12 r-θ planes were measured along the z-direction. The synchronization was the same as that used for the central zone in the cooler exit. The parameters are shown in Table B–4. For some planes in which the flow exhibited large velocity gradients, two measurements with two different times between laser pulses were performed to fully capture high and low velocity regions.

Table B–4: PIV parameters in the cover

N°	1	2	3	4	5	6	7	8	9	10	11	12
Height (mm)	28	48	68	88	108	128	148	168	188	208	228	248
TBP (μs)	30	30, 80	30, 80	25, 80	25, 80	20, 60	20, 60	30	35	35	35	40

Air gap and interpole region

In this region, 12 different r-θ planes were measured. The parameters are presented in Table B–5. Moreover, three different synchronizations were used for each one to measure three different interpoles (see Fig. 5–18), summarized in Table B–6.

Table B–5: PIV parameters for the interpole and air gap region

Duct number	Height (mm)	TBP (μs)
2	85.0	15
4	133.6	15
6	182.2	10
9	255.1	10
11	303.7	10
13	352.3	10
17	449.4	10
19	498.0	15
21	546.6	15
24	619.5	15
26	668.0	15
28	716.6	12

Table B–6: Trigger delay in the interpole region

	Interpole	Air gap
Central zone	25694.1875	27916.3875
Leading side	36805.1875	39027.3875
Lagging side	42360.6875	44582.8875

References

[1] R. J. Adrian. Scattering Particle Characteristics and Their Effect on Pulsed Laser Measurements of Fluid Flow : Speckle Velocimetry vs Particle Image Velocimetry. *Applied Optics*, 23(11):1690–1691, 1984.

[2] R. J. Adrian. Twenty Years of Particle Image Velocimetry. *Experiments in Fluids*, 39(2):159–169, 2005.

[3] R. J. Adrian and J. Westerweel. *Particle Image Velocimetry*. Cambridge University Press, 2011.

[4] E. Bach. Procédure de calibration piv. Technical report, Hydro-Québec, 2014.

[5] A. Boglietti, A. Cavagnino, D. Staton, M. Shanel, M. Mueller, and C. Mejuto. Evolution and Modern Approaches for Thermal Analysis of Electrical Machines. *Industrial Electronics, IEEE Transactions on Industrial Electronics*, 56(3):871–882, 2009.

[6] F. L. Bookstein. Principal Warps: Thin-Plate Splines and the Decomposition of Deformations. *IEEE Transactions on pattern analysis and machine intelligence*, 11(6):567–585, 1989.

[7] M. Chaaban, J. Leduc, C. Hudon, and D. N. Nguyen. Thermal Behaviour of Large Hydro-Generators. In *International Symposium on Transport Phenomena and Dynamics of Rotating Machinery*, page 154, 2008.

[8] R. Depraz, R. Zickermann, A. Schwery, and F. Avellan. CFD Validation and Air Cooling Design Methodology for Large Hydro Generator. *Proc. 17th ICEM*, pages 1–6, 2006.

[9] J. H. Ferziger and M. Perić. *Computational methods for fluid dynamics*, volume 3. Springer Berlin, 2002.

[10] V. Filipan, R. Budin, and A. Mihelic-Bogdanic. Air Flow Measurement on Hydro Generators. *Water Power and Dam Construction*, 45(1):44–46, 1993.

[11] L. Gui, S. T. Wereley, and Y. H. Kim. Advances and Applications of the Digital Mask Technique in Particle Image Velocimetry Experiments. *Measurement Science and Technology*, 14(10):1820, 2003.

[12] N. Gunabushanam and J. Venkata Sureh. Experimental and CFD Analysis of Hydrogenerator Ventilation Components. In *CIGRE, International Councilof large electric systems*, 2006.

[13] E. Hartono. Experimental Study of Air Flow in a Hydro Power Generator Model. Master's thesis, Chalmers University of Technology, 2011.

[14] E. Hartono, M. Golubev, P. Moradnia, V. Chernoray, and H. Nilsson. A PIV Study of The Cooling Air Flow in An Electric Generator Model. Technical report, Department of Applied Mechanics, Chalmers University of Technology, 2012.

[15] G. Hemery and T. Kunz. Performance improvements of hydro generators due to advanced ventilation calculations. Technical report, Alstom Hydro, 2009.

[16] C. Hudon, F. Torriano, J.-F. Morissette, A. Merkhouf, M. Chaaban, S. Belanger, J. Leduc, F. Lafleur, C. Millet, and M. Gagné. Hydro Generator Multi-Physic Modeling. *European Journal of Electrical Engineering*, 13:563–589, 2010.

[17] M. Ishikawa, Y. Murai, A. Wada, M. Iguchi, K. Okamoto, and F. Yamamoto. A Novel Algorithm for Particle Tracking Velocimetry Using the Velocity Gradient Tensor. *Experiments in fluids*, 29(6):519–531, 2000.

[18] C. J. Kähler, B. Sammler, and J. Kompenhans. Generation and Control of Tracer Particles for Optical Flow Investigations in Air. *Experiments in Fluids*, 33:736–742, 2002.

[19] R. D. Keane and R. J. Adrian. Theory of Cross-Correlation Analysis of PIV Images. *Applied Scientific Research*, 49(3):191–215, 1992.

[20] J. Kompenhans and J. Reichmuth. Particle Imaging Velocimetry in a Low Turbulent Wind Tunnel and Other Facilities. In *Proceedings of the IEEE Montech'86 conference*. AGARD conference, October 1986.

[21] W. T. Lai, D. C. Bjorkquist, M. P. Abbott, and A. A. Naqwi. Video Systems for PIV Recording. *Measurement Science and Technology*, 9(3):297–308, 1998.

[22] J. P. Lallemand, R. Desailly, and C. Froehly. Mesure de Vtesse dans un Liquide par Diffusion Cohere´ nte. *Acta Astronautica*, 4(3):343–356, 1977.

[23] N. Lancial, F. Torriano, F. Beaubert, S. Harmand, and G. Rolland. Study of a Taylor-Couette-Poiseuille Flow in an Annular Channel with Slotted Rotor. In *Proccedings of the XXIth International Conference on Electrical Machines (ICEM), Berlin, Germany*, pages 1422–1429, 2014.

[24] S. Laskin. Submerged Aerosol Unit. AEC Project Quaterly Report UR-38, Univiversity of Rochester, 1948.

[25] S. Lemay. Étude Exprimentale de l'Écoulement dans le Eanal Inter-Aube d'une Turbine de Type Bulbe. Master's thesis, Universit Laval, 2014.

[26] C. D. Meinhart, S. T. Wereley, and J. G. Santiago. A PIV Algorithm for Estimating Time-Averaged Velocity Fields. *Journal of Fluids Engineering*, 122:285–289, 2000.

[27] R. Meynart. Equal Velocity Fringes in a Rayleigh-Benard Flow by a Speckle Method. *Applied Optics*, 19(9):1385–1386, 1980.

[28] R. Meynart. Digital Image Processing for Speckle Flow Velocimetry. *Review of Scientific Instruments*, 53:110–111, 1982.

[29] R. Meynart. Instantaneous Velocity Field Measurements in Unsteady Gas flow by Speckle Velocimetry. *Applied optics*, 22(4):535–540, 1983.

[30] R. Meynart. Speckle Velocimetry : an Application of Image Analysis Techniques to the Measurement of Instantaneous Velocity Fields in Unsteady Flow. In *Proceedings of the International Congress on Instrumentation in Aerospace Simulation Facilities*. ICIASF, IEEE record, September 1983.

[31] R. Meynart. Speckle Velocimetry Study of Vortex Pairing in a Low-Re Unexcited Jet. *Physics of Fluids*, 26(8):2074–2079, 1983.

[32] P. Moradnia, V. Chernoray, and H. Nilsson. Experimental and Numerical Investigation of the Cooling Air Flow in an Electric Generator. In *HEFAT2011, 8th International Conference on Heat Transfer, Fluid Mechanics and Thermodynamics*, pages 242–249, 2011.

[33] K. Okamoto, Y. A. Hassan, and W. D. Schmidl. New Tracking Algorithm for Particle Image Velocimetry. *Experiments in Fluids*, 19(5):342–347, 1995.

[34] M. Raffel, Willert C., and J. Kompenhans. *Particle Image Velocimetry: a Practical Guide*. Springer, 2007.

[35] A. Sciacchitano, B. Wieneke, and F. Scarano. PIV Uncertainty Quantification by Image Matching. *Measurement Science and Technology*, 24:045302, 2013.

[36] S. M. Soloff, R. J. Adrian, and Z.-C. Liu. Distortion Compensation for Generalized Stereoscopic Particle Image Velocimetry. *Measurement Science and Technology*, 8(12):1441–1454, 1997.

[37] X. Song, F. Yamamoto, M. Iguchi, and Y. Murai. A New Tracking Algorithm of PIV and Removal of Spurious Vectors using Delaunay Tessellation. *Experiments in Fluids*, 26(4):371–380, 1999.

[38] S. L. Soo, C.L. Tien, and V. Kadambi. Determination of Turbulence Characteristics of Solid Particles in a Two-Phase Stream by Optical Autocorrelation. *Review of Scientific Instruments*, 30:821–824, 1959.

[39] D.A. Staton and A. Cavagnino. Convection heat transfer and flow calculations suitable for analytical modelling of electric machines. In *IEEE Industrial Electronics, IECON 2006-32nd Annual Conference on*, pages 4841–4846. IEEE, 2006.

[40] M. A. Sutton, W. J. Wolters, W. H. Peters, W. F. Ranson, and S. R. McNeill. Determination of Displacements using an Improved Digital Correlation Method. *Image and Vision Computing*, 1(3):133–139, 1983.

[41] F. Torriano, N. Lancial, M. Lévesque, G. Rolland, C. Hudon, F. Beaubert, J.-F. Morissette, and S. Harmand. Heat Transfer Coefficient Distribution on the Pole Face of a Hydrogenerator Scale Model. *Applied Thermal Engineering*, 70:153–162, 2014.

[42] K. Toussaint. Caractérisation de l'Écoulement d'Air dans une Maquette d'Alternateur Hydroélectrique par Méthodes Numérique et Expérimentale. Master's thesis, Ecole Polytechnique de Montréal, 2011.

[43] K. Toussaint, F. Torriano, J.-F. Morissette, C. Hudon, and M. Reggio. CFD Analysis of Ventilation Flow for a Scale Model Hydrogenerator. In *ASME 2011 Power Conference collocated with JSME ICOPE 2011*, pages 627–637. American Society of Mechanical Engineers, 2011.

[44] J. Westerweel. Efficient Detection of Spurious Vectors in Particle Image Velocimetry Data. *Experiments in Fluids*, 16(3-4):236–247, 1994.

[45] J. Westerweel. Fundamentals of Digital Particle Image Velocimetry. *Measurement Science and Technology*, 8(12):1379–1392, 1997.

[46] J. Westerweel and F. Scarano. Universal Outlier Detection for PIV Data. *Experiments in Fluids*, 39(6):1096–1100, 2005.